A disproportionate impact of G9a methyltransferase deficiency on the X chromosome

Attila Szanto,[1,2] Rodrigo Aguilar,[1,2] Barry Kesner,[1,2] Roy Blum,[1,2] Danni Wang,[1,2] Catherine Cifuentes-Rojas,[1,2] Brian C. del Rosario,[1,2] Katalin Kis-Toth,[3] and Jeannie T. Lee[1,2]

[1]Department of Molecular Biology, Massachusetts General Hospital, Boston, Massachusetts 02114, USA; [2]Department of Genetics, The Blavatnik Institute, Harvard Medical School, Boston, Massachusetts 02115, USA; [3]Department of Rheumatology, Beth Israel Deaconess Medical Center, Harvard Medical School Boston, Massachusetts 02115, USA

G9a is a histone methyltransferase responsible for the dimethylation of histone H3 at lysine 9 (H3K9me2). G9a plays key roles in transcriptional silencing of developmentally regulated genes, but its role in X-chromosome inactivation (XCI) has been under debate. Here, we uncover a female-specific function of G9a and demonstrate that deleting G9a has a disproportionate impact on the X chromosome relative to the rest of the genome. G9a deficiency causes a failure of XCI and female-specific hypersensitivity to drug inhibition of H3K9me2. We show that G9a interacts with Tsix and Xist RNAs, and that competitive inhibition of the G9a-RNA interaction recapitulates the XCI defect. During XCI, Xist recruits G9a to silence X-linked genes on the future inactive X. In parallel on the future Xa, Tsix recruits G9a to silence *Xist* in *cis*. Thus, RNA tethers G9a for allele-specific targeting of the H3K9me2 modification and the G9a-RNA interaction is essential for XCI.

[*Keywords*: G9a; H3K9me2; Tsix; X chromosome inactivation; Xist; epigenetics; noncoding RNA]

Supplemental material is available for this article.

Received February 12, 2020; revised version accepted May 27, 2021.

G9a is a widely expressed histone methyltransferase enzyme with a conserved SET domain (Tachibana et al. 2001) and functions as a heteromeric complex with G9a-like protein (GLP). G9a and GLP possess the same substrate specificity and function as the main histone 3 lysine 9 (H3K9) methyltransferases in vivo (Tachibana et al. 2002, 2005, 2008). While H3K9me3 is crucial for silencing of pericentromeric heterochromatin and is regulated by Suv39h1/2, the mono- and dimethylation induced by G9a/GLP are mainly associated with transcriptional repression of euchromatin (Tachibana et al. 2002; Peters et al. 2003; Rice et al. 2003). G9a is critical for embryonic development and multiple lineage commitments during differentiation and is also responsible for various aspects of tumorigenesis (Shinkai and Tachibana 2011; Shankar et al. 2013). Loss of G9a in mice results in embryonic lethality (E9.5–E12.5) (Tachibana et al. 2002), and in vitro, G9a-deficient embryonic stem (ES) cells exhibit severe differentiation defects due to attenuated silencing of pluripotency genes *Oct-3/4* and *Nanog* (Feldman et al. 2006).

Although chromatin immunoprecipitation high-throughput sequencing (ChIP-seq) studies show that G9a deposits H3K9me2 mark at specific genomic locations, the basis of G9a's locus-specific recruitment is not yet understood. Multiple interacting proteins have been reported to localize G9a to specific chromatin loci (Shinkai and Tachibana 2011), and it was also suggested to be recruited by long noncoding RNAs (ncRNAs) Kcnq1ot1 and Airn to the *Kcn1* and *Igf2r* loci, respectively, to silence multiple genes in *cis* during the epigenetic process of genomic imprinting (Nagano et al. 2008; Pandey et al. 2008). However, the role of G9a as an RNA-binding protein and the mechanisms underlying its epigenetic silencing have not been systematically addressed to date.

The role of ncRNAs has been intensively studied in the epigenetic silencing process of X-chromosome inactivation (XCI), a mechanism used by mammals to balance X-chromosome gene dosages between the two sexes (Starmer and Magnuson 2009; Wutz 2011; Disteche 2012; Lee 2012; Dupont and Gribnau 2013; Schulz and Heard 2013; Jégu et al. 2017). During early development, female cells randomly choose one X chromosome for inactivation. XCI is controlled by an X-linked region called the X-inactivation center (Xic) that is known for harboring

Corresponding author: lee@molbio.mgh.harvard.edu
Article published online ahead of print. Article and publication date are online at http://www.genesdev.org/cgi/doi/10.1101/gad.337592.120.

multiple ncRNA genes, including *Xist* (Brockdorff et al. 1992; Brown et al. 1992) and *Tsix* (Lee and Lu 1999; Lee et al. 1999). Before XCI, Xist is not expressed but becomes up-regulated during XCI only from the inactive X (Xi), where it initiates chromosome-wide silencing as it blankets the Xi in *cis* (Clemson et al. 1996). Xist is negatively regulated by an antisense transcript Tsix (Lee et al. 1999), and disruption of *Tsix* results in impaired designation of the active X (Xa) (Lee and Lu 1999), failure to repress *Xist*, and consequent elevation of Xist expression (Lee and Lu 1999; Sado et al. 2001, 2005; Morey et al. 2004; Shibata and Lee 2004; Ohhata et al. 2008). The expression and spread of Xist through the Xi involves recruitment of silencing factors that establish and maintain the Xi (Wutz 2011; Disteche 2012; Lee 2012; Jégu et al. 2017). Two major repressive marks of Xi are H3K9 and histone 3 lysine 27 (H3K27) methylation (Heard et al. 2001; Wang et al. 2001; Boggs et al. 2002; Mermoud et al. 2002; Peters et al. 2002; Plath et al. 2003; Silva et al. 2003; Kohlmaier et al. 2004).

While the mechanism of H3K27 methylation has been studied extensively, much less is known about the role of H3K9 methylation during XCI. The available literature presents conflicting views. For instance, various studies suggest that H3K9 methylation is reported to be an early marker of XCI (Heard et al. 2001; Boggs et al. 2002; Mermoud et al. 2002; Peters et al. 2002). Another study has also identified CDYL as an XCI-related protein and suggests that CDYL binds to the Xi through the H3K27me3 and H3K9me2 mark, thereby implicating G9a and the associated H3K9me2 mark in XCI (Escamilla-Del-Arenal et al. 2013). On the other hand, the exact role of G9a and H3K9me2 remains uncertain. For one, some earlier studies used H3K9me2 antibodies with variable specificity and potential for cross-reactivity to other histone marks such as H3K27me3 (Silva et al. 2003). Uncertainty was further introduced by a report in which it was shown that Xist expression and maintenance of XCI in G9a-deficient embryos were unaffected (Ohhata et al. 2004), even as a G9a conditional knockout showed derepressed X-linked genes in male cells (Yokochi et al. 2009). Thus, the question of whether G9a affects XCI remains unsettled by the early studies. Here, using epigenomic technologies, we further explore the role of G9a during XCI and demonstrate that G9a is an RNA-binding protein with a disproportionate impact on the X chromosome in female cells.

Results

A female-specific differentiation defect in G9a$^{-/-}$ *ES cells*

Using CRISPR technology, we generated female G9a knockout ES cells using *Tsix*$^{TST/+}$ (Ogawa and Lee 2003) as a parental line. The resulting knockout (*G9a*$^{-/-}$) cells showed a complete loss of G9a expression in two independent clones and decreased total H3K9me2 (Fig. 1A). We confirmed the deletion of G9a by loss of G9a immunostaining (Fig. 1B; Supplemental Fig. S1A,B) and concurrent loss of H3K9me2 immunostaining (Supplemental Fig. S1C,D). However, there was some residual H3K9me2 (Fig. 1A), consistent with the idea that other H3K9 methyltransferases could possibly compensate for the deletion of G9a (Tachibana et al. 2005). When differentiated in vitro, we observed a striking difference between *G9a*$^{-/-}$ versus control *G9a*$^{+/+}$ (in the *Tsix*$^{TST/+}$ background) cells (Fig. 1C). Every *G9a*$^{-/-}$ clone tested showed a significant defect in embryoid body (EB) outgrowth between days 4 and 10 of differentiation (Fig. 1C; Supplemental Fig. S2). Consistent with poor outgrowth, cell proliferation assays showed a significant decrease in number of mutant versus normal cells at each test time point (Fig. 1D). The proliferation defect was also observed when comparing *G9a*$^{-/-}$ versus *G9a*$^{+/+}$ cells in a *Tsix*$^{+/+}$ background (16.7, wild type [WT]) (Fig. 1D). Interestingly, this early differentiation defect was observed only in female but not in male *G9a*$^{-/-}$ cells (Fig. 1C), which showed a similar level of outgrowth in comparison with wild-type (J1) controls (Tachibana et al. 2002). We conclude that there is a female-specific ES cell differentiation defect when G9a is ablated.

G9a is required to regulate both Tsix *and* Xist

Before XCI, female ES cells possess two active Xs (Xa) but can be induced to undergo XCI when differentiated in culture (Brown and Willard 1994; Beard et al. 1995). The female-specific defect observed in *G9a*$^{-/-}$ cells suggests a potential problem with XCI. During differentiation of female ES cells, Xist RNA is up-regulated, and the transcripts cluster into a "cloud" of Xi-associated particles (Clemson et al. 1996; Sunwoo et al. 2015). Although H3K9me2 was suggested previously to be enriched on the Xi (Heard et al. 2001; Escamilla-Del-Arenal et al. 2013), here we could not detect enrichment of either G9a or its H3K9me2 mark by immunofluorescence (Supplemental Fig. S1A,C). However, an absence of cytological enrichment would not exclude a role for G9a during XCI.

Notably, Xist clouds appeared either smaller or less intense in the *G9a*$^{-/-}$ cells (Fig. 1E; Supplemental Fig. S1B, D). To investigate the dynamics of Xist cloud formation, we performed Xist and Tsix RNA-FISH in *G9a*$^{+/+}$ and *G9a*$^{-/-}$ cells (Fig. 1E,F; Supplemental Fig. S1). In *G9a*$^{+/+}$ cells, Tsix is initially expressed from both X chromosomes but becomes down-regulated on the future Xi while persisting on the future Xa. In these *G9a*$^{+/+}$ cells, we introduced a heterozygous *Tsix* truncation mutation (*Tsix*$^{TST/+}$). The nonfunctional truncated Tsix transcript on the *Mus musculus musculus* (mus) X chromosome predestines this allele to become the Xi during cell differentiation. Thus, in the *G9a*$^{+/+}$ cells, the X chromosome of *Mus musculus castaneus* (cas) origin (with a wild-type *Tsix* allele) is invariably the Xa (Fig. 1E,F; Ogawa and Lee 2003). We performed RNA-FISH using probes that could detect both wild-type and truncated Tsix RNA (probe is proximal to the truncation site). In *G9a*$^{-/-}$ cells, there was a measurable but small increase in the number of nuclei showing persistent biallelic Tsix expression. There was also a small but significant decrease in the number of nuclei with proper Xist clouds (Fig. 1E,F). Interestingly, Tsix

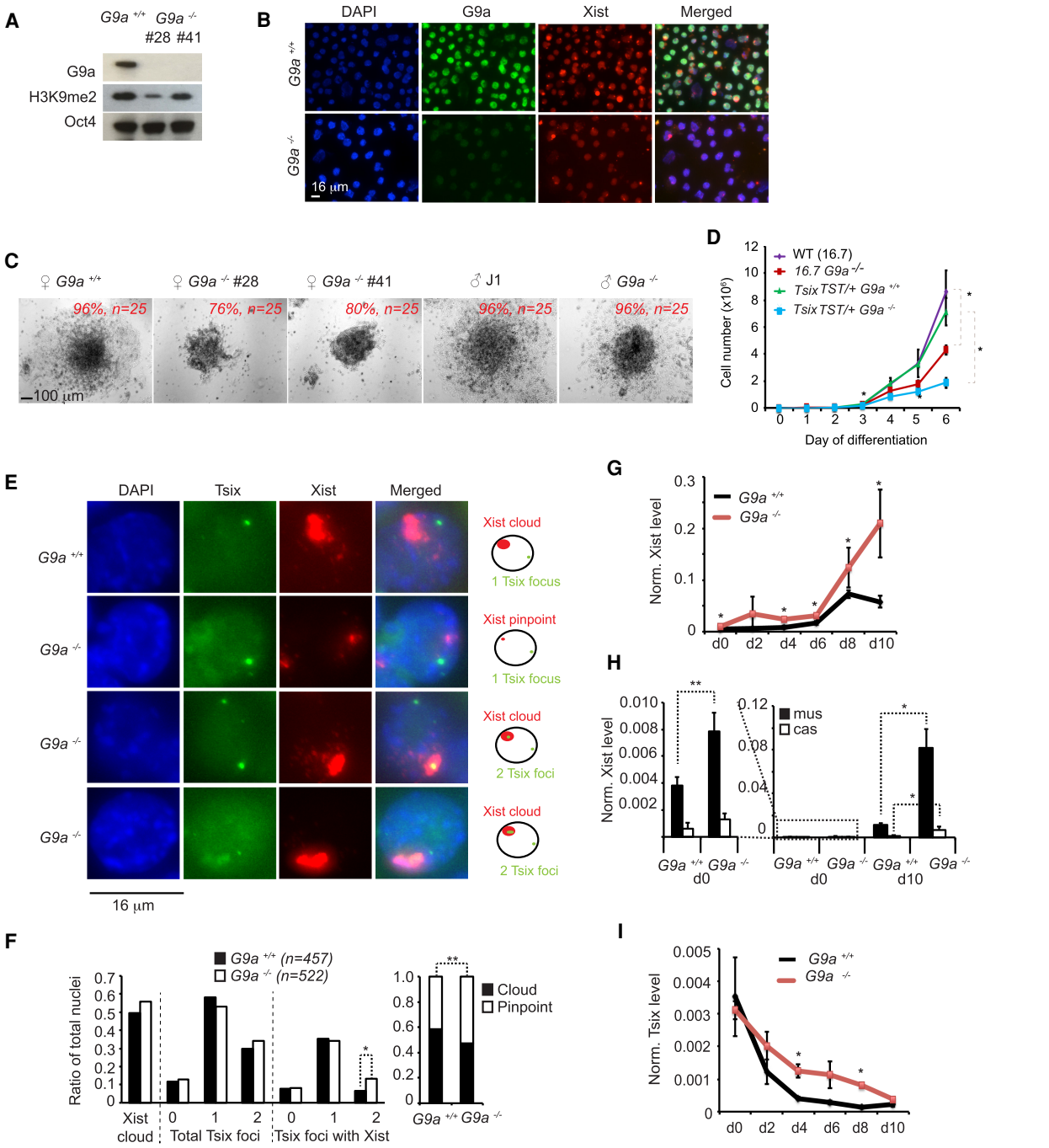

Figure 1. G9a deletion results in a female-specific differentiation defect. (*A*) Western blot shows the expression of G9a in control $G9a^{+/+}$ ($Tsix^{TST/+}$) cells and in two independent $G9a^{-/-}$ clones. H3K9me2 and OCT4 (control) are also shown. (*B*) G9a immunostaining combined with Xist RNA-FISH was performed in female d10 $G9a^{+/+}$ and $G9a^{-/-}$ differentiated cells. Representative fields are shown. (*C*) Microscopic images of representative embryoid bodies (EBs) after 4 d of differentiation in suspension and 2 d on gelatin. $Tsix^{TST/+}$ ($G9a^{+/+}$) is the parental line, and #28 and #41 are two independent $G9a^{-/-}$ clones. As controls, wild-type male J1 ES cells and male $G9a^{-/-}$ ES cells were used. Percentages of EBs (with sample size, *n*) showing the phenotype (either a normal outgrowth or no outgrowth) are indicated in red text for each genotype. See Supplemental Figure S2 for additional examples at various differentiation days. (*D*) Cell proliferation assay. The number of cells for each genotype was counted on the indicated day of ES differentiation. (*) $P < 0.05$, as determined by Student's *t*-test comparing $G9a^{+/+}$ versus $G9a^{-/-}$ clones in either a WT (16.7) or $Tsix^{TST/+}$ background. $n = 3$ biological replicates. (*E*) Representative images of Tsix and Xist RNA-FISH in $G9a^{-/-}$ and parental controls. Schematic drawings of the FISH results shown next to each panel. (*F*) Quantitation of results from *D*. (*) $P < 0.013$, (**) $P < 0.0004$ based on χ^2 test. (*G*) RT-qPCR of Xist levels in female control and $G9a^{-/-}$ cells during differentiation. $n = 3$–9. (*) $P < 0.05$. (*H*) Allele-specific RT-qPCR result of Xist level in undifferentiated (d0) and differentiated (d10) female ES cells. The *left* panel is zoomed into the *right* one to show d0. $n = 3$. (*) $P < 0.05$, (**) $P < 0.01$. (*I*) RT-qPCR of Tsix levels in female control and $G9a^{-/-}$ cells during differentiation. $n = 3$–9. (*) $P < 0.05$.

could often be detected together within a large Xist domain, suggesting a failure of *Tsix* silencing. Together with the female-specific differentiation defect, these data provided the first hint of a problem with XCI.

We also examined Xist dynamics by reverse transcription and quantitative polymerase chain reaction (RT-qPCR). Oddly, there was an increase in Xist expression overall (Fig. 1G,H), despite a decrease in the number of Xist clouds (Fig. 1E,F). This observation suggests an improper localization of Xist RNA to the Xi in the absence of G9a. Such localization defects have been observed in other contexts where Xist is highly expressed but cannot bind normally to the Xi (Sarma et al. 2010; Jeon and Lee 2011; Sunwoo et al. 2017; Colognori et al. 2019). Similarly, Tsix expression remained higher during differentiation in the G9a-deficient cells (Fig. 1I). Taking advantage of the single-nucleotide polymorphisms between the mus and cas chromosomes, we performed allele-specific RT-qPCR to quantitate the differences. With allele-specific primers, we found that Xist expression was elevated from both X chromosomes in pre-XCI mutant cells (Fig. 1H, left). During differentiation, the Xist up-regulation occurred predominantly from the mus X chromosome—the future Xi (Fig. 1H, right). Significantly, however, Xist was also detected from future Xa in mutant cells. These results suggest that Xist expression is under the control of G9a in both pre-XCI cells and cells undergoing XCI. Collectively, these findings uncover a dysregulation of *Tsix* and *Xist* in cells deficient for G9a.

Loss of G9a causes aberrant Xi silencing

Given the *Tsix/Xist* dysregulation, we next performed transcriptomic analysis to examine changes in genome-wide versus X-linked gene expression in G9a-deficient cells. On a genome-wide basis, some genes increased in expression and others decreased, as expected when epigenetic factors are ablated (Fig. 2A,B; Supplemental Table S1). Specifically, in undifferentiated cells, G9a deletion resulted in up-regulation of 665 and down-regulation of 539 genes. In differentiated cells, 762 genes were up-regulated, and 992 genes were down-regulated. Pathway analysis suggested that, in undifferentiated ES cells, G9a deletion affected the expression of genes involved primarily in morphogenesis, neuronal development, cell signaling, and cell death (Fig. 2A, left). In differentiated ES cells, enriched pathways included organ development and tissue morphogenesis (Fig. 2A, right). These data position G9a as an important regulator of embryonic development.

Interestingly, among genome-wide changes in differentiated cells, the X chromosome stood out. When analyzing bulk X-linked gene expression (Xa + Xi combined), there were twice as many aberrantly up-regulated X-linked genes than the autosome-wide average, and the number of down-regulated X-linked genes was two to three times lower than the autosomal average (Fig. 2B,C). Among 1478 annotated X-linked genes in the mm9 annotation of the mouse genome, only 404 were expressed in ES cells (Fig. 2D). Of these, 67 showed significantly increased expression, while only 19 showed a decrease. On the other hand, there was not a major difference for chr13. The difference in the number of DEGs between chrX and chr13 was significant (χ^2 test, $P = 0.0062$). The difference in cumulative distribution profiles between bulk chrX and chr13 genes was also significant (Fig. 2E). These bulk analyses indicate that X-linked genes were up-regulated relative to autosomal genes, but they do not provide information about which allele was up-regulated. Analyzing genes in bulk also does not yield the sensitivity or specificity that allelic analyses generally provide.

To determine whether the Xa or Xi was affected, we analyzed the data allele-specifically using three biological replicates each of $G9a^{+/+}$ and $G9a^{-/-}$ clones. We calculated the degree of allelic skewing (AS) using the ratio (cas − mus)/(cas + mus), where a value of +1 indicated absolute skewing of expression in favor of the cas allele, while −1 indicated absolute skewing to the mus allele, and zero represented equal expression from the two alleles. Among 1478 X-linked genes, 392 have allelic information. Among the 392 genes, 203 genes were expressed (RPKM > 0.5). Of expressed X-linked genes, 117 showed cas (Xa) bias ($P < 0.05$) in $G9a^{+/+}$ cells on d10. In $G9a^{-/-}$ cells, cas (Xa) skewing was seen in only 66 genes. This difference (117 vs. 66) is highly significant ($P = 0.0088$, χ^2 test). Thus, 43.5% of expressed cas-biased genes (51/117) showed reactivation in the absence of G9a.

Cumulative distribution plots (CDPs) showed a significant right shift (more genes with higher expression) when comparing differentially expressed genes upon G9a deletion on chrX versus chr13 (Fig. 2E). When allelic skew of all genes with *cas*-biased expression in the control were compared, a significant shift down in the $G9a^{-/-}$ cells indicated insufficient silencing of the Xi (Fig. 2F). Heat map analysis showed that most of the genes were expressed biallelically (no significance difference upon G9a deletion) in $G9a^{+/+}$ cells on chrX and 13 on d0, prior to XCI, as expected (Fig. 2G). Similarly, scatter plot analysis of individual genes demonstrated a clustering at AS = 0 (Supplemental Fig. S3). In contrast, establishment of XCI in d10 $G9a^{+/+}$ ES cells resulted in skewing of alleles to favor *cas* expression, occurring only on chrX and not chr13 (Fig. 2G; Supplemental Fig. S3). When G9a was ablated, the red shift was significantly less robust for chrX ($P < 0.001$) (Fig. 2G, bottom bar graphs), and scatter plot analysis showed a clear deviation from AS = 0 (Supplemental Fig. S3). These general trends were also evident in allele-specific CDPs of allelic ratios (Fig. 2H). Finally, allele-specific RNA-seq coverage tracks of three X-linked genes, *Pim2*, *Idh3g*, and *Dkc1*, exemplified the loss of Xi gene silencing in the absence of G9a (Fig. 2I).

Thus, we conclude that ~40% of X-linked genes do not undergo proper XCI in the absence of G9a. The overall number of affected genes is similar to those observed for mutants of other XCI-related factors, including SMCHD1 or Polycomb complexes, and mutants of specific Xist domains affecting interactions with key protein partners such as BRG1 (Blewitt et al. 2008; Gendrel et al. 2012; Wang et al. 2018; Colognori et al. 2019; Jégu et al. 2019; Nesterova et al. 2019).

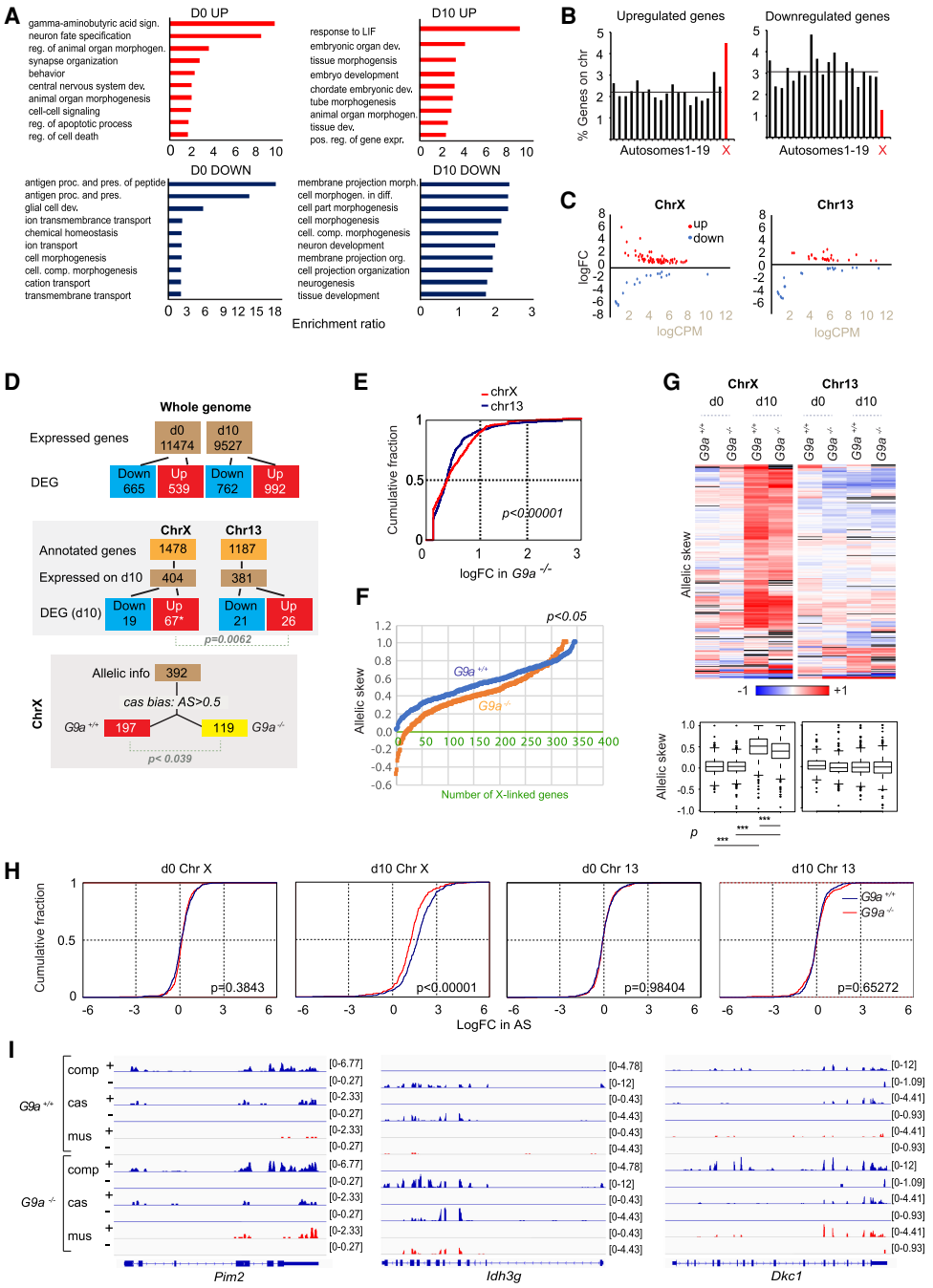

Figure 2. Up-regulation of X-linked gene expression following G9a ablation. (*A*) Pathway analysis to present significantly enriched biological processes upon G9a deletion ($P < 0.05$, FDR < 0.05). (*B*) Percentage of genes on each chromosome being up-regulated (*top*) or down-regulated (*bottom*) in d10 $G9a^{-/-}$ compared with control cells. Line indicates autosomal median (3.09 for down-regulated and 2.16 for up-regulated genes). (*C*) Scatter plot shows the distribution of genes on chrX (*top*) or chr13 (*bottom*), whose expression was significantly changed ($P < 0.05$, min 1.5×) in d10 ES cells between control and $G9a^{-/-}$ cells. Log fold change is plotted against relative expression level (logCPM). (CPM) Counts per million reads. (*D*) Diagram shows the number of genes expressed in day 0 and day 10, number of differentially expressed genes (DEGs; $P < 0.05$, min. 1.5×), and number of analyzed genes on chrX and 13 (*top*); number of annotated genes on chrX and chr13, number of expressed genes in differentiated cells, and DEGs (*middle*; this difference in the number of DEGs between chrX and chr13 is significant; χ^2 test, $P = 0.00662$); and number of genes on chrX with allelic information, genes with cas-biased expression in differentiated cells, and number of G9a-sensitive genes in terms of allelic skew (*bottom*). *P*-value is based on χ^2 test. (*E*) Cumulative density plot shows the difference between chr13- and chrX-linked genes (bulk inclusive of both mus and cas alleles) being induced in $G9a^{-/-}$ cells. *P*-value was calculated using Mann–Whitney test. (*F*) Allelic skew values for all (348) cas-biased genes on chrX are plotted and sorted by value. $P = 0.039$ based on Wilcoxon test. (*G*, *top*) Heat map presents the allelic skew (cas − mus)/(cas + mus) of gene expression on chrX and chr13 in d0 and d10 $G9a^{+/+}$ and $G9a^{-/-}$ cells. (*Bottom*) Box plots of the above allelic skew with the indicated *P*-values based on a Student's *t*-test. (***) $P \ll 0.001$. (*H*) Cumulative density plots of cas/mus allelic ratios between $G9a^{+/+}$ and $G9a^{-/-}$ cells indicate d0 and d10 differences on chrX and chr13. *P*-values were calculated using Mann–Whitney test. (*I*) IGV tracks show allele-specific RNA-seq coverage of representative X-linked genes in differentiated $G9a^{+/+}$ and $G9a^{-/-}$ cells.

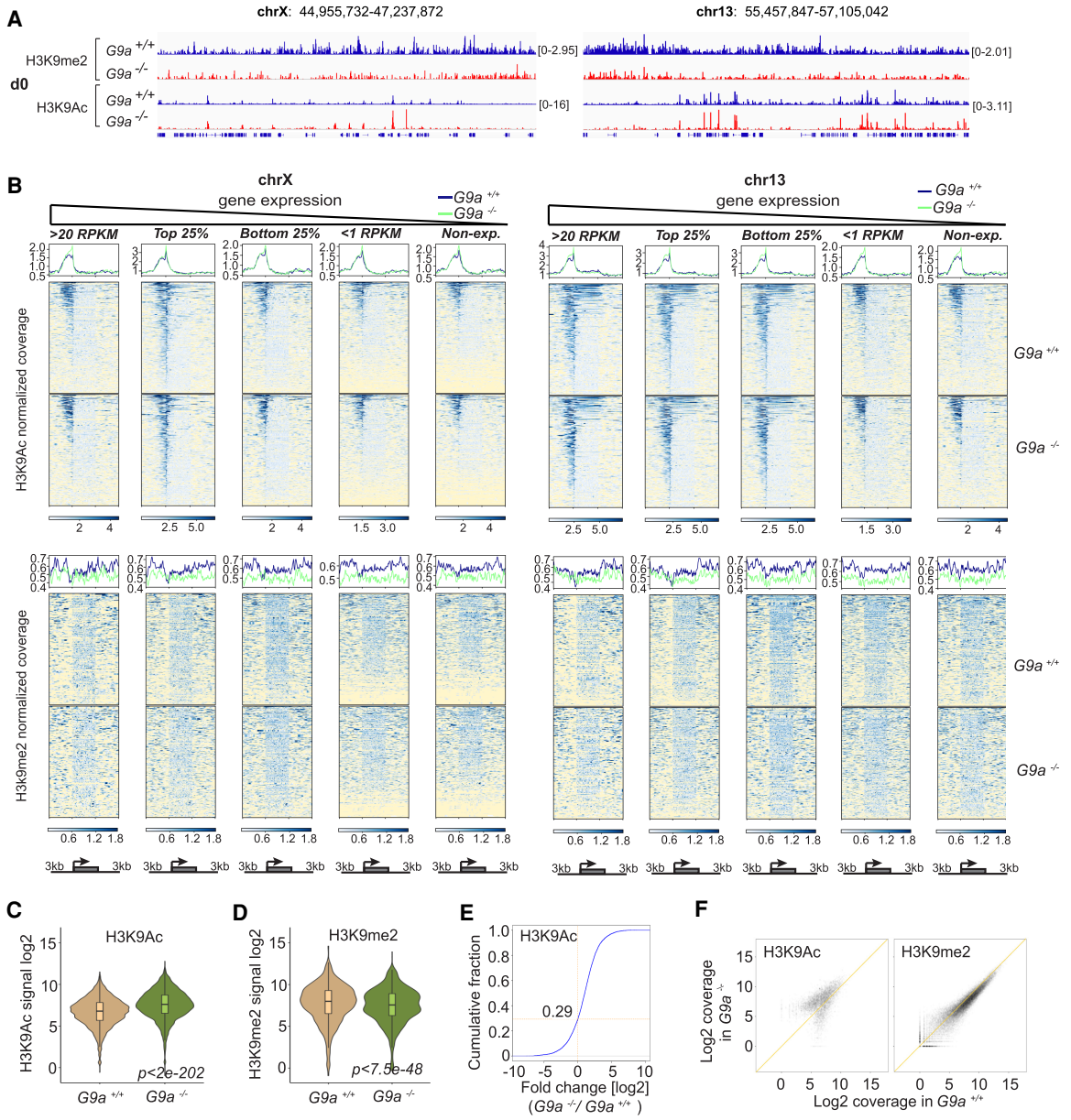

Figure 3. Genome-wide impact of G9a deficiency on H3K9me2 and H3K9Ac in day 0 female ES cells. (*A*) IGV tracks illustrate H3K9me2 and H3K9Ac coverages across a 4500-kb region of chrX (*left*) and chr13 (*right*) in undifferentiated (day 0) $G9a^{+/+}$ and $G9a^{-/-}$ cells. (*B*) H3K9Ac (*top*) and H3K9me2 (*bottom*) ChIP-seq metagene profiles and heat maps of normalized coverages relative to their expression level on chrX (*left*) and chr13 (*right*). Four RPKM quartiles are analyzed along with a category of genes with no expression (Non-exp). (*C*,*D*) Violin plots for log2 H3K9Ac (*C*) and H3K9me2 (*D*) coverages over promoters (TSS ± 1 kb) for d0 $G9a^{-/-}$ versus $G9a^{+/+}$ cells show a significant increase when G9a is depleted. $P < 2 \times 10^{-202}$ or $P < 7.5 \times 10^{-48}$, respectively, Mann–Whitney test. (*E*) Cumulative frequency plot of $\log_2$ fold change in $G9a^{-/-}$ versus $G9a^{+/+}$ cells on day 0. Note the right shift, with 71% of genes showing increased H3K9Ac (cumulative fraction = 0.29). (*F*) Log_2 input-normalized coverages for H3K9Ac (*left*) and H3K9me2 (*right*) in $G9a^{-/-}$ versus $G9a^{+/+}$ cells on day 0.

Disproportionate impact of G9a deficiency on the X chromosome relative to autosomes

Because G9a is responsible for the H3K9me2 mark, we performed ChIP-seq to determine how the mark was affected by G9a loss. Analysis of two biological replicates showed good correlation (Supplemental Fig. S4). In accordance with Western blot results (Fig. 1A), ChIP-seq revealed a global decrease, but not complete loss, of genomic H3K9me2 in day 0 $G9a^{-/-}$ cells (Fig. 3A). However, ChIP-seq analysis also unveiled several findings that were not evident in the bulk H3K9me2 quantitation. First, the deficiency of H3K9me2 was more prominent in day 0 cells as compared with day 10 cells, although a deficit (albeit smaller) persisted on day 10 (Fig. 3A; Supplemental Fig. S5A). Second, H3K9me2 characteristically

marked broad regions rather than defined peaks, as shown by metagene plots (Fig 3B; Supplemental Fig. S5B). The partial recovery of H3K9me2 in day 10 cells support the notion of a compensatory H3K9me2 mechanism and suggests a selective pressure in differentiating cells to use alternative H3K9me2 silencing mechanisms to survive. Nevertheless, H3K9me2 was not fully restored during differentiation, and a disparity persisted in day 10 cells on both X chromosomes and autosomes.

We then performed ChIP-seq analysis of H3K9 acetylation (H3K9Ac), an active mark with an opposing and mutually exclusive relationship to H3K9me2 at the promoters (Tachibana et al. 2002; Peters et al. 2003; Rice et al. 2003). Analysis of two biological replicates showed good correlation (Supplemental Fig. S4). At a global level, the H3K9Ac pattern shows two types of differences in the $G9a^{-/-}$ cells versus the $G9a^{+/+}$ parental control: Pre-existing acetylation peaks increased, and new peaks appeared where there previously were none (Fig. 3A, bottom panels; Supplemental Fig S5A). We performed a metagene analysis for genes grouped by their expression levels (RPKM) in four separate quartiles (Fig. 3B; Supplemental Fig. S5B). In $G9a^{+/+}$cells, as expected, H3K9me2 was enriched over genes in the lowest quartile (<1 RPKM) for both chr13 and chrX. This quartile was the most sensitive to G9a loss, as evidenced by the increased H3K9Ac enrichment, but even genes in other expressed quartiles and nonexpressed genes showed an increase (Fig. 3B; Supplemental Fig. S5B). Metagene profiles indicated an overall dip in H3K9me2 at the promoters where H3K9Ac peaks were seen (Fig 3B; Supplemental Fig. S5B). This anticorrelation was especially evident in the top two quartiles and held true in both day 0 and 10 cells. Overall, G9a-deficient cells showed a significant decrease of H3K9me2 across gene bodies and a concurrent increase in H3K9Ac peaks over promoters, irrespective of quartiles (Fig. 3C,D; Supplemental Fig. S5C,D). Consistent with this, CDP analysis showed an overall right shift in $\log_2$FC (0.29 on day 0; 0.54 on day 10) for H3K9Ac (Fig. 3E; Supplemental Fig. S5EF), and scatter plot analysis showed an upward deviation from the diagonal (Fig. 3F). Together, these data demonstrate an inverse correlation between H3K9me2 and H3K9Ac for both Xs and autosomes.

To distinguish Xa from Xi cells undergoing XCI, we performed an allele-specific analysis in day 10 cells. The mm9 assembly lists 1478 X-linked genes in the mouse genome, of which 972 genes provided a minimum of five allele-specific reads for H3K9me2. A total of 446 genes showed Xi bias in $G9a^{+/+}$ cells, as expected {allelic skewing defined as the difference in the allelic coverage [AS = (cas − mus)/(cas + mus)], with +1 indicating absolute skewing in favor of Xa, −1 indicating absolute skewing to Xi, and zero representing allelic equality}. On the other hand, 271 showed H3K9Ac favoring Xa, as expected.

To assess impact when G9a was ablated, we performed allelic analysis in two biological replicates for both H3K9me2 and H3K9Ac ChIP-seq and examined changes in cumulative distribution plots (CDPs). Xi showed a significant upward shift in H3K9me2 skewing in $G9a^{-/-}$ cells, indicating that there was a greater impact on the mus (Xi) alleles than on cas (Xa) (Fig. 4A). On the other hand, there was a significant downward shift for H3K9Ac in $G9a^{-/-}$ cells, indicating that acetylation increased disproportionately on mus (Xi) relative to cas (Xa) (Fig. 4B). The opposing trends for H3K9me2 and H3K9Ac are consistent with the two marks being mutually exclusive. Overall, the disproportionate effects on Xi relative to Xa argue that the Xi is more affected by G9a loss than the Xa or any other chromosome.

The disproportionate effects were in fact even more pronounced when we considered only those genes that are significantly differentially marked by G9a. In wild-type cells, 67 X-linked genes qualified as mus-biased with a cumulative binomial distribution probability of $P < 0.05$. Among these, only 15 genes maintained such bias when G9a was ablated. Thus, 78% of these asymmetrically marked genes lost H3K9me2. Using the same criteria, 265 genes showed significant cas bias for H3K9Ac in wild-type cells. Among them, only 108 genes remained biased after G9a deletion. Biological replicates showed similar results: From 61 H3K9me2 mus-biased genes in the wild type, only 11 remained biased in $G9a^{-/-}$; from 186 H3K9Ac cas-biased genes, only 88 remained in the $G9a^{-/-}$ (Fig. 4C,D). These data demonstrate again that G9a has a disproportionate impact on Xi relative to Xa.

Metagene analysis revealed a similar trend. Analysis of overall coverage profiles showed that the difference occurred across gene bodies for H3K9me2, whereas it occurred predominantly at promoters for H3K9Ac (Fig. 4E, top and middle). Notably, both Xa and Xi were affected by G9a depletion, but CDP analysis showed that a significantly greater effect was observed for the Xi (Fig. 4E, bottom). Overall, 244 genes had >1.5-fold decreased H3K9me2 on the Xi in $G9a^{-/-}$ cells, whereas only 141 showed higher H3K9me2 and the others remained unchanged (Supplemental Table S2). Out of 244 genes with decreased H3K9me2, nearly all (230/244) showed higher acetylation on Xi in $G9a^{-/-}$ cells (Supplemental Table S2). For acetylation overall, 463 genes showed >1.5×-fold increased acetylation on Xi in $G9a^{-/-}$ cells, whereas only 155 genes showed lower acetylation (Supplemental Table S2). These changes corresponded to a significant increase in gene expression from the Xi (mus) relative to Xa (cas) in G9a-deficient cells on day 10 (Fig. 4F).

Thus, G9a deletion inversely changes the balance of methylation and acetylation on Xi and, in doing so, perturbs gene repression on the Xi. This was also the case at the X-inactivation center. The *Tsix* promoter was acetylated biallelically, whereas *Xist* lacked acetylation and had H3K9me2 (Fig. 4G). In $G9a^{-/-}$ cells, however, acetylation increased at the *Xist* promoter on both alleles. Most importantly, this increased acetylation occurred also on the Xa at the *Xist* promoter on day 10 (Fig. 4G), suggesting failure of *Xist* silencing on the Xa. ChIP-qPCR performed on additional replicates corroborated the findings (Supplemental Fig. S5G,H), with *Magea2* serving as a positive control (Tachibana et al. 2002). Collectively, our data demonstrate an impact of G9a loss on XCI and reveal *Tsix* and *Xist* as targets of G9a-dependent methylation.

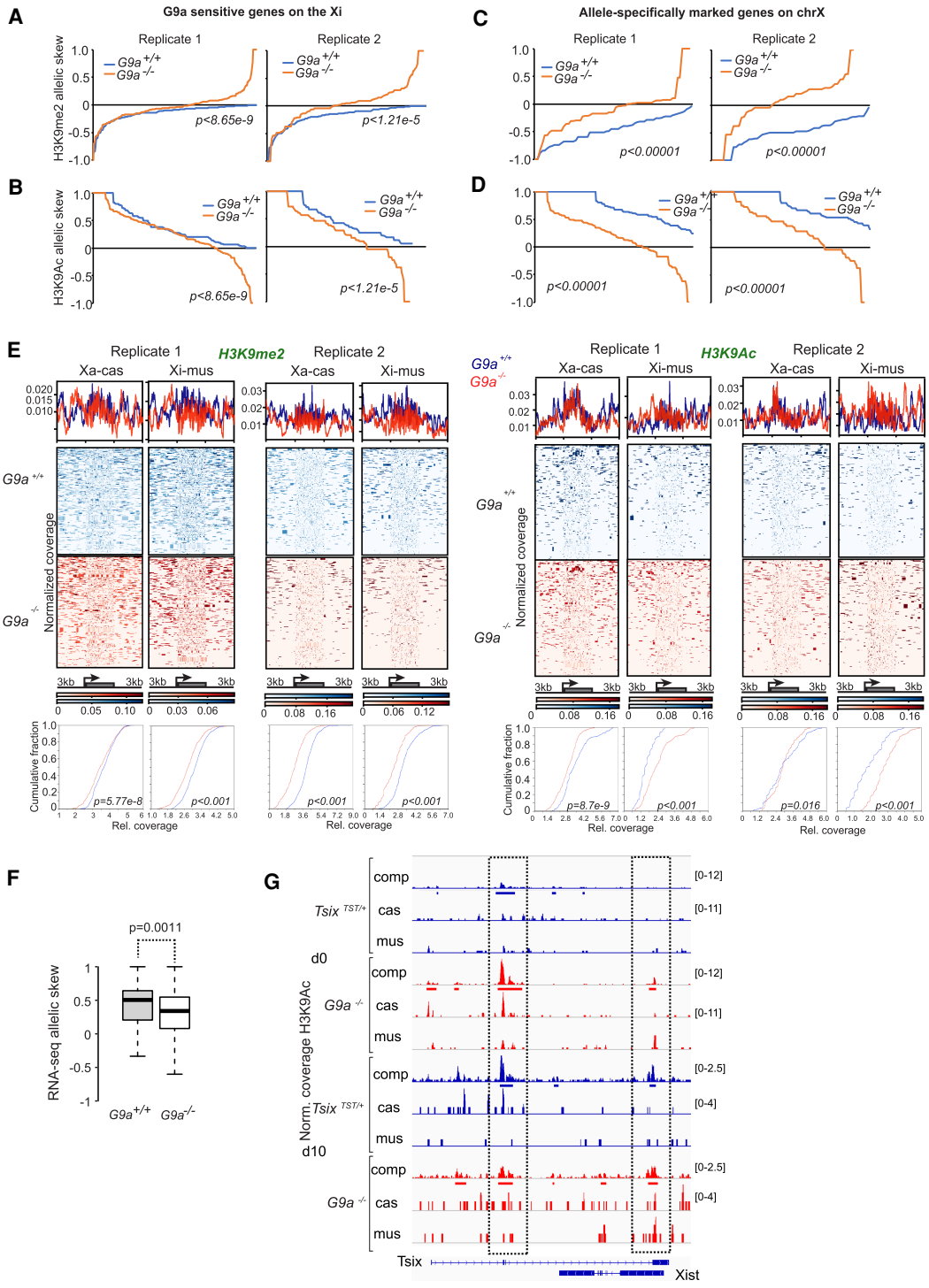

Figure 4. Allele-specific changes in H3K9me2 and H3K9Ac upon G9a deletion on chrX. (*A*,*B*) Impaired allelic skew in d10 $G9a^{-/-}$ versus $G9a^{+/+}$ cells based on Xi (mus)-skewed H3K9me2 (*A*) or Xa (cas)-skewed H3K9Ac (*B*) in control cells. Genes were selected based on difference in AS values. *P*-values are based on Wilcoxon test. Two biological replicates (1,2) are shown. (*C*,*D*) Impaired allelic skew in d10 $G9a^{-/-}$ versus $G9a^{+/+}$ cells based on significant allelically skewed H3K9me2 (*C*) or H3K9Ac (*D*). Genes were selected based on cumulative binomial distribution probability ($P < 0.05$) calculated from allelic coverage and on allelic bias. *P*-values are based on Wilcoxon test. Two biological replicates are shown. (*E*) H3K9me2 (*left*) and H3K9Ac (*right*) coverage profiles over Xa and Xi genes in $G9a^{+/+}$ (blue) and $G9a^{-/-}$ (red) cells. Metagenes (*top*), normalized coverage tracks for individual X-linked genes (*middle*), and CDPs for H3K9me2 gene body coverage and H3K9Ac promoter coverage (*bottom*) are shown. Two biological replicates (1 and 2) shown for each. (*F*) A significant increase in gene expression from the Xi (mus) relative to Xa (cas) in G9a-deficient cells is shown by a drop in RNA allelic skew. Included in analysis were genes with a more than twofold increase in H3K9Ac on the Xi after G9a depletion, and loci with a >1.5-fold decrease in H3K9me2 on the Xi allele. $P = 0.0011$ by the Mann–Whitney test. (*G*) IGV tracks of normalized composite coverages (comp or all reads) or allele-specific coverages (mus or cas) for H3K9Ac over the *Tsix/Xist* locus. $G9a^{+/+}$ versus $G9a^{-/-}$ cells are shown for undifferentiated (d0) and differentiated (d10) states. Boxes highlight differences in the promoter regions after G9a deletion.

G9a binds Xist and Tsix RNAs

G9a has been shown to interact with Kcnq1ot1 and Airn, two transcripts within imprinted gene clusters (Nagano et al. 2008; Pandey et al. 2008). Given G9's effect on XCI, we asked whether G9a could bind XCI regulators as well. We performed cross-linked RNA immunoprecipitation (UV-RIP) using a G9a-specific antibody or IgG as a negative control (Fig. 5A). Indeed, in parent control cells, both Xist and Tsix RNAs were enriched in the G9a pull-downs. Kcnq1ot1 was also enriched in our hands. In contrast, neither cyclophilin A RNA nor U1 showed enrichment. The enrichment of Xist, Tsix, and Kcnq1ot1 was abolished in *G9a*$^{-/-}$ cells, demonstrating a specificity of the binding. These data indicate that G9a interacts with Xist and Tsix RNAs.

Next, we expressed and purified G9a protein from baculovirus-infected Sf9 cells (Fig. 5B). In vitro histone methyltransferase assays demonstrated that the purified protein was catalytically active (Fig. 5C, PRC2-positive control). In vitro RNA pull down assays using purified G9a and purified total ES cellular RNA revealed some degree of enrichment for Xist and Kcnq1ot1, but not negative control U1 RNA, among this complex pool of cellular RNAs (Fig. 5E). RNAs transcribed from two G9a target loci, Kis2 and Rian, also showed modest enrichment. However, Tsix RNA did not in this assay.

To map preferred binding domains within each transcript, we in vitro transcribed various RNA fragments and performed RNA-binding assays (Fig. 5D,F). Xist fragments containing repeats A and C (pXE1 and pXE9) showed significant enrichment. Similarly, Tsix also preferentially bound G9a within the repeats A and C regions (RepA and RepC). To validate these interactions, we carried out RNA electrophoretic mobility shift assays (EMSAs) using purified protein and RNA fragments. In multiple independent experiments, Tsix RepA and RepC fragments showed a shift with G9a protein, but not with green fluorescent protein (GFP) or glutathione S-transferase (GST) negative control proteins (Fig. 5G,H; Supplemental Fig. S6). Xist RepA also showed a shift with G9a, but not with GFP or GST (Fig. 5G,H; Supplemental Fig. S6). In contrast, G9a could not shift negative control β-actin (ActB) or maltose-binding protein (MBP) RNA (Fig. 5G, H; Supplemental Fig. S6). Dose-response densitometry revealed a quantitative difference between G9a versus GFP binding, as the fraction bound to G9a was 10 times higher relative to GFP (Fig. 5I). These findings suggest that G9a interacts with Xist and Tsix through two repeat motifs, RepA and RepC. However, we note that the degree of interaction was overall variable and modest, indicating that the interactions may be transient in nature or that other factors might be required for stable interactions inside cells. Because RepA has also been shown to interact with PRC2 (Zhao et al. 2008; Cifuentes-Rojas et al. 2014; Davidovich et al. 2015) and G9a likewise also interacts with PRC2 (Mozzetta et al. 2014; Maier et al. 2015), there could be an interplay between G9a and PRC2 at RepA. Increasing G9a levels actually reduced the RepA shift by PRC2 (Fig. 5J, top), whereas addition of the GFP negative control protein had no effect (Fig. 5J, bottom). The neutralization of the PRC2–RepA shift could be owing to an antagonism between the two proteins or, alternatively, to formation of a larger multifactor complex that is too large to migrate into the gel.

To look for functional interaction between G9a and XCI, we reasoned that if H3K9 dimethylation on the Xi was driven by Xist RNA's recruitment of G9a, we would expect localization of Xist and the H3K9me2 mark on a chromosome-wide scale. Indeed, analysis of Xist CHART data (Simon et al. 2013) and our H3K9me2 ChIP-seq data demonstrated well-correlated Xist and H3K9me2 coverages across the Xi (Pearson's $r = 0.6396$) in differentiating female ES cells (Fig. 5H). This correlation was on par with Xist's correlation with EZH2 ($r = 0.5727$), consistent with the idea that PRC2 and G9a complex with each other. Interestingly, however, Xist's correlation with PRC2's mark H3K27me3 was considerably higher on the Xi ($r = 0.9677$). This difference between H3K27me3 and H3K9me2 likely reflects the overall higher coverage of H3K27me3 across the Xi relative to H3K9me2. We conclude that G9a can physically interact with Xist and Tsix RNAs, although the interaction may be transient or weak in an in vitro setting.

Disrupting G9a–RNA interaction recapitulates the G9a$^{-/-}$ *phenotype*

In addition to PRC2 and G9a (as shown here), repeat A has been shown to interact with other protein factors as well, including the RNA helicase ATRX (Sarma et al. 2014), the megadalton protein SPEN (Chu et al. 2015; McHugh et al. 2015; Minajigi et al. 2015), and RNA methylation protein RBM15 (Patil et al. 2016; Nesterova et al. 2019). Repeat A may thus serve as a hub for a large number of XCI factors, including G9a. We would therefore predict that blocking the interaction of repeat A with essential proteins such as G9a would have significant physiological effects on XCI. We wished to test this idea in a way that would circumvent issues associated with transient transfection during a multiday course of cell differentiation. We therefore developed an in vivo knockoff system to perturb the RNA–protein interactions through competitive inhibition. In this system, we stably overexpressed RepA or RepC under a doxycycline (dox)-inducible promoter to outcompete interactions with the endogenous the endogenous Xist RNA domains.

Dox induction was robust in every case (Fig. 6A,B). In multiple biological replicates, ChIP-qPCR showed that overexpressing the competing RNA fragments led to significantly decreased H3K9me2 at the *Tsix* promoter and 5′ end of *Xist* (Fig. 6C,D; Supplemental Fig. S7), whereas the *Magea2* control did not exhibit any change in H3K9me2 (Fig. 6E; Supplemental Fig. S7C). Finally, overexpression of the competing RNA fragments phenocopied the growth and differentiation defect of the G9a-deficient female ES cells (Fig. 1B vs. 6F). RNA-FISH revealed concurrent defects in XCI, as evidenced by retention of biallelic Tsix expression and failure of Xist up-regulation (Fig. 6G). Taken together, our findings argue that

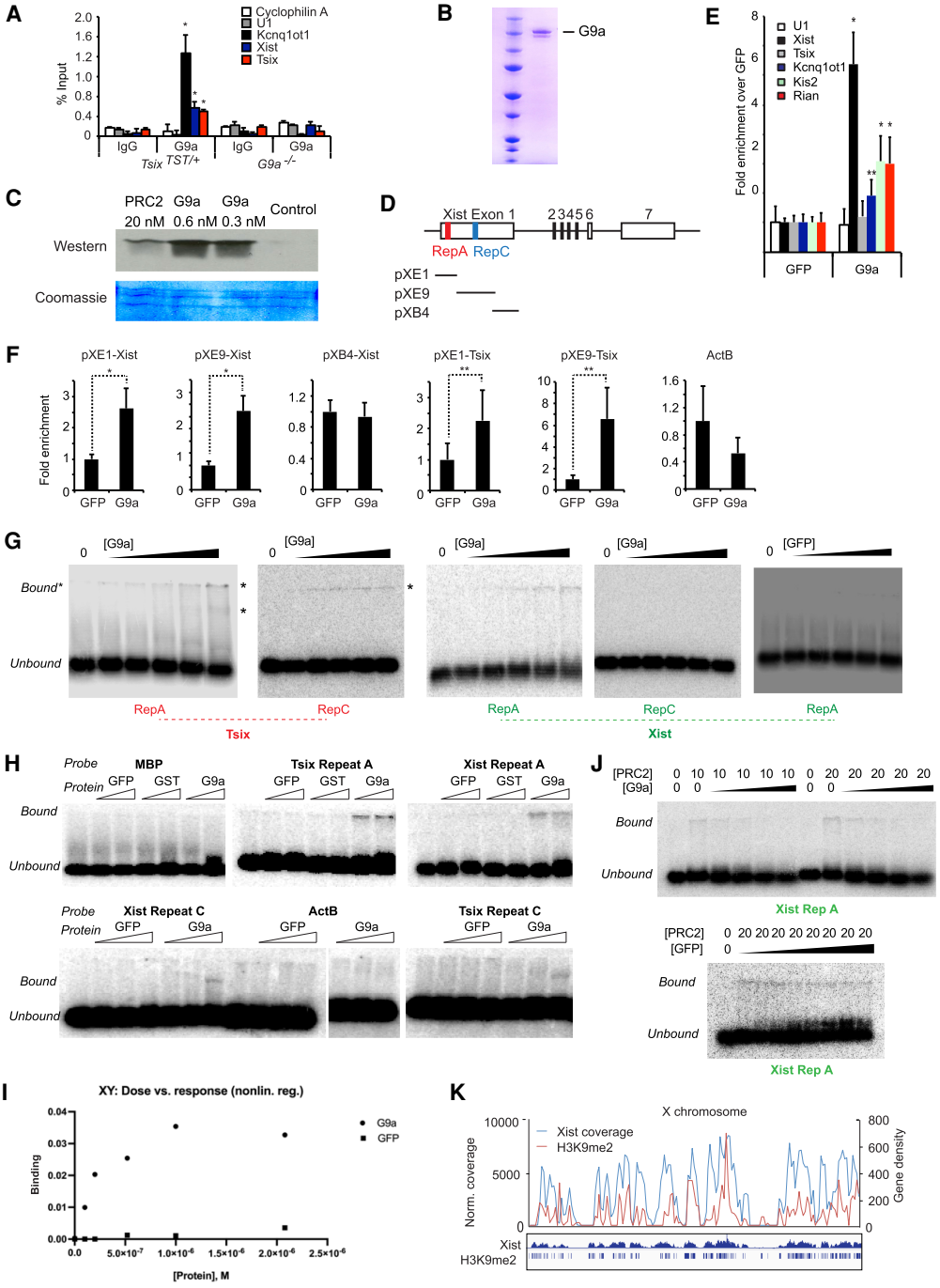

Figure 5. G9a specifically interacts with Xist and Tsix RNAs. (*A*) UV-RIP was performed in control and *G9a*$^{-/-}$ cells using IgG or G9a antibodies. RNAs pulled down were analyzed by RT-qPCR, and the relative levels are shown. (*B*) Coomassie staining of acrylamide gel shows purified FLAG-G9a from Sf9 cells. (*C*) Autoradiogram of histone methyltransferase assay performed on control PRC2 of purified G9a proteins and negative control. Coomassie staining is shown as loading control. (*D*) Schematic representation of Xist/Tsix to show the RNA fragments used for in vitro binding experiments. (*E*) In vitro RNA pull-down was performed using purified GFP or G9a proteins and total RNA from d0 and d10 ES cells. RT-qPCR was used to quantitate enriched RNAs. (*F*) In vitro RNA binding was performed using the indicated in vitro transcribed RNA fragments (20 pmol) and purified GFP or G9a. RNAs were quantitated using RT-qPCR, and the fold enrichments over the GFP are shown. (*G*) Autoradiogram of RNA EMSA experiments. Xist or Tsix repeat A or repeat C, or ActB probes were used to bind increasing concentrations (100, 200, 520, 1040, and 2080 nM) of purified G9a or GFP. Bound (*) and unbound RNA probes are as marked. (*H*) Autoradiogram of RNA EMSA experiments. Xist or Tsix repeat A, repeat C, or negative control MBP ActB probes were used to bind increasing concentrations of purified G9a, GST, or GFP. Bound and unbound RNA probes are as marked. (*I*) Densitometric analysis of protein–RNA binding in EMSA experiments. Titration of G9a or GFP against 20 pmol of RepA probe for the experiments in *G*. (*J*) Autoradiogram of three-component EMSA experiments. (*Top*) PRC2–RepA interaction was tested against increasing concentrations (50, 100, 250, and 500 nM) of G9a protein. PRC2, 10 or 20 nM as indicated. RepA at 10 pM. (*Bottom*) PRC2–RepA interaction was tested against increasing concentrations of GFP at 1, 2, 4, 10, 20, 40, and 100 nM. (*K*) Distribution of Xist RNA coverage (CHART in blue) over chrX correlates with G9a-specific H3K9me2-ed genes (red) in day 10 female ES cells.

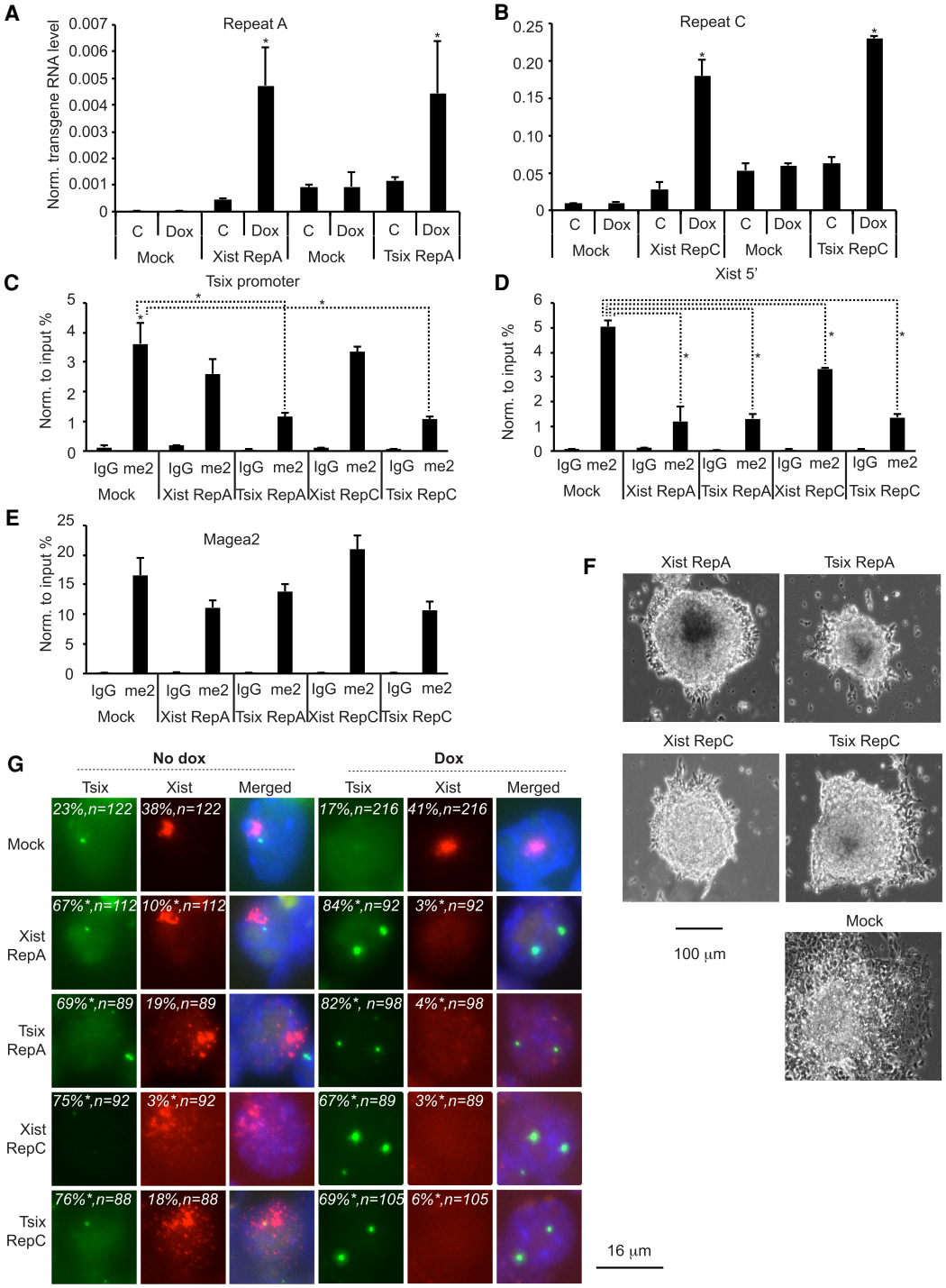

Figure 6. Competitive inhibition of G9a–RNA interactions perturbs XCI in female cells. (*A*,*B*) Expression of indicated RNA fragments was assessed by RT-qPCR after 24 h of induction with 1 mg/mL doxycycline or vehicle (PBS; $n = 3$). (*) $P < 0.05$. (*C*–*E*) Cells were differentiated in the absence or presence of 1 mg/mL doxycycline for 6 d, and ChIP was performed. Enrichment was quantitated with Q-PCR at the indicated regions ($n = 3$). (*) $P < 0.05$. (*F*) Microscopic images of embryoid bodies after 6 d of differentiation and doxycycline treatment. (*G*) RNA-FISH for Tsix and Xist was performed in the vehicle or doxyxcycline-treated cells after 6 d of differentiation. DAPI was used for nuclear staining.

disrupting RepA and RepC interactions recapitulates the XCI defects and failed cell differentiation in G9a-ablated female cells. Although the data are also consistent with an inhibition of other interacting proteins (PRC2, SPEN, RBM15), these other proteins are not known to be H3K9 dimethylases. Thus, the disruption of H3K9

dimethylation argues that G9a is competitively inhibited and plays a crucial histone-modifying function for XCI through RepA and RepC.

Pharmacological inhibition of H3K9 dimethylation recapitulates the XCI defect

To further test the idea that the histone methyltransferase activity of G9a is critical for spreading of Xi gene silencing, we turned to pharmacological inhibitors of G9a's methyltransferase activity. The small molecule inhibitors UNC0638 (UNC) (Guler et al. 2017) and BIX01294 (BIX) (Kubicek et al. 2007) have been shown to have selective inhibition of H3K9 dimethylation. In ES cells, we found that both inhibitors decreased global H3K9me2 (Fig. 7A). UNC's effect was especially strong, demonstrating a stronger depletion than the G9a knockout. UNC treatment even resulted in H3K9me2 depletion in a $G9a^{-/-}$ background. These observations are consistent with the presumption that other H3K9 methyltransferases, such as GLP (Vedadi et al. 2011), could compensate for G9a's absence.

We then determined the effect of UNC and BIX treatment on XCI. In control male ES cells, neither drug had an obvious effect on cell differentiation and outgrowth of EBs (Fig. 7B; Supplemental Fig. S8A). On the other hand, the drugs severely affected the outgrowth of female ES cells (Fig. 7B; Supplemental Fig. S8A). The effect was even more dramatic when $G9a^{-/-}$ female cells were treated with the H3K9me2 inhibitors, with cells not only failing to outgrow but actively dying during differentiation. In contrast, $G9a^{-/-}$ male cells continued to grow and resisted cell death (Fig. 7B; Supplemental Fig. S8A). Altogether, H3K9me2 inhibitors phenocopied the effect of G9a deletion, with an even stronger phenotype when drug treatment occurred in a $G9a^{-/-}$ background. RNA-FISH showed blunted Xist clusters in UNC-treated control female cells, phenocopying the G9a deficiency (Fig. 7C,D). Interestingly, however, the dearth of full Xist clouds was not owing to failure of Xist expression, as the steady-state RNA levels appeared unchanged in UNC-treated female cells undergoing differentiation (Fig. 7E). This was also the case in $G9a^{-/-}$ female cells (Fig. 7E). Thus, the failure of G9a recruitment to the Xi is not due to inability to express Xist in either drug-treated or G9a-deficient cells. UNC and BIX yielded similar results (Fig. 7D; Supplemental Fig. S8B–E), but the H3K9me3 inhibitor, chaetocin, did not cause this female-specific effect (Supplemental Fig. S8B,C). These data demonstrate the specificity for H3K9me2 and G9a's physiological relevance for XCI. The female-specific hypersensitivity and the nearly complete loss of surviving cells provide evidence for the essential nature of Xist-mediated recruitment of G9a and G9a-mediated H3K9me2 during the establishment of XCI.

Discussion

To elucidate the role of G9a and H3K9me2 during XCI, here we have created $G9a^{-/-}$ female ES cells and systematically investigated the contribution of the H3K9me2 mark during XCI. We found that female cells are hypersensitive to G9a loss, and pharmacologically blocking the H3K9 dimethylation causes a severe growth defect. Ablating G9a disproportionately affects X-linked genes and results in a failure of Xist-mediated gene silencing. We also found that G9a makes contact with noncoding RNAs, as is now observed to be the case for many epigenetic modifiers (Lee 2012; Melé and Rinn 2016). During XCI, Xist recruits G9a to silence X-linked genes on the future Xi, whereas Tsix recruits G9a to silence Xist on the future Xa. RNA-mediated recruitment is likely to require additional factors inside cells in order to stabilize the interaction, given that G9a by itself only has a modest affinity for Xist and Tsix RNA in vitro (Fig. 5). Perturbing the RNA–G9a interaction recapitulates the XCI defect. We therefore conclude that G9a plays a critical role during XCI and that RNA tethers G9a for allele-specific targeting of the H3K9me2 modification.

In the absence of G9a, ~40% of genes with Xa-biased expression demonstrate improper silencing (51 out of 117 Xi genes; Fig. 2D). This percentage is on par with the partial loss of XCI resulting from mutations in other crucial XCI factors. For example, ablation of SMCHD1, a key regulator of the 3D Xi structure, led to defects in Xist spreading and heterochromatin formation. RNA-seq identified 73 SMCHD1-sensitive genes—a failure to silence 40% of expressed X-linked genes (Wang et al. 2018). Similarly, a deletion of *Xist*'s repeat B compromised Polycomb recruitment, Xist spreading, and silencing of ~35% of expressed X-linked genes (Colognori et al. 2019). When *Pcgf3* (PRC1) was also deleted, only 99 genes lost silencing on the Xi (Almeida et al. 2017). These findings underscore the fact that the Xi has multiple parallel mechanisms of silencing and that, apart from *Xist*, mutating any other single gene has ever been shown to fully compromise XCI. Our current study elucidates G9a as one of the crucial pathways converging on full Xi silencing.

Our current findings can be placed in the context of the existing models (Fig. 7F). Prior to XCI, Tsix RNA is expressed biallelically, and this expression inhibits *Xist* induction and the initiation of XCI (Lee et al. 1999). An allelic choice mechanism then selects one Xa and one Xi in a mutually exclusive manner. On the future Xa, Tsix persists at high levels and continues to block *Xist* induction (Lee and Lu 1999; Ohhata et al. 2008). Our present work indicates that Tsix RNA recruits G9a to dimethylate H3K9 at the 5′ end of *Xist*, contributing to the lockdown of *Xist* silencing on the future Xa. On the future Xi, Tsix expression is lost, enabling the full up-regulation of Xist RNA (Lee and Lu 1999; Luikenhuis et al. 2001; Stavropoulos et al. 2001; Ohhata et al. 2008). Xist RNA then binds YY1 within an essential nucleation site in *cis* prior to spreading along the X chromosome (Jeon and Lee 2011). As Xist spreads, it both recruits silencers to and repels activators from the X chromosome (Zhao et al. 2008; Chu et al. 2015; McHugh et al. 2015; Minajigi et al. 2015; Moindrot et al. 2015; Monfort et al. 2015; Jégu et al. 2019). Our current study suggests that Xist comes into physical contact with and recruits G9a, resulting in

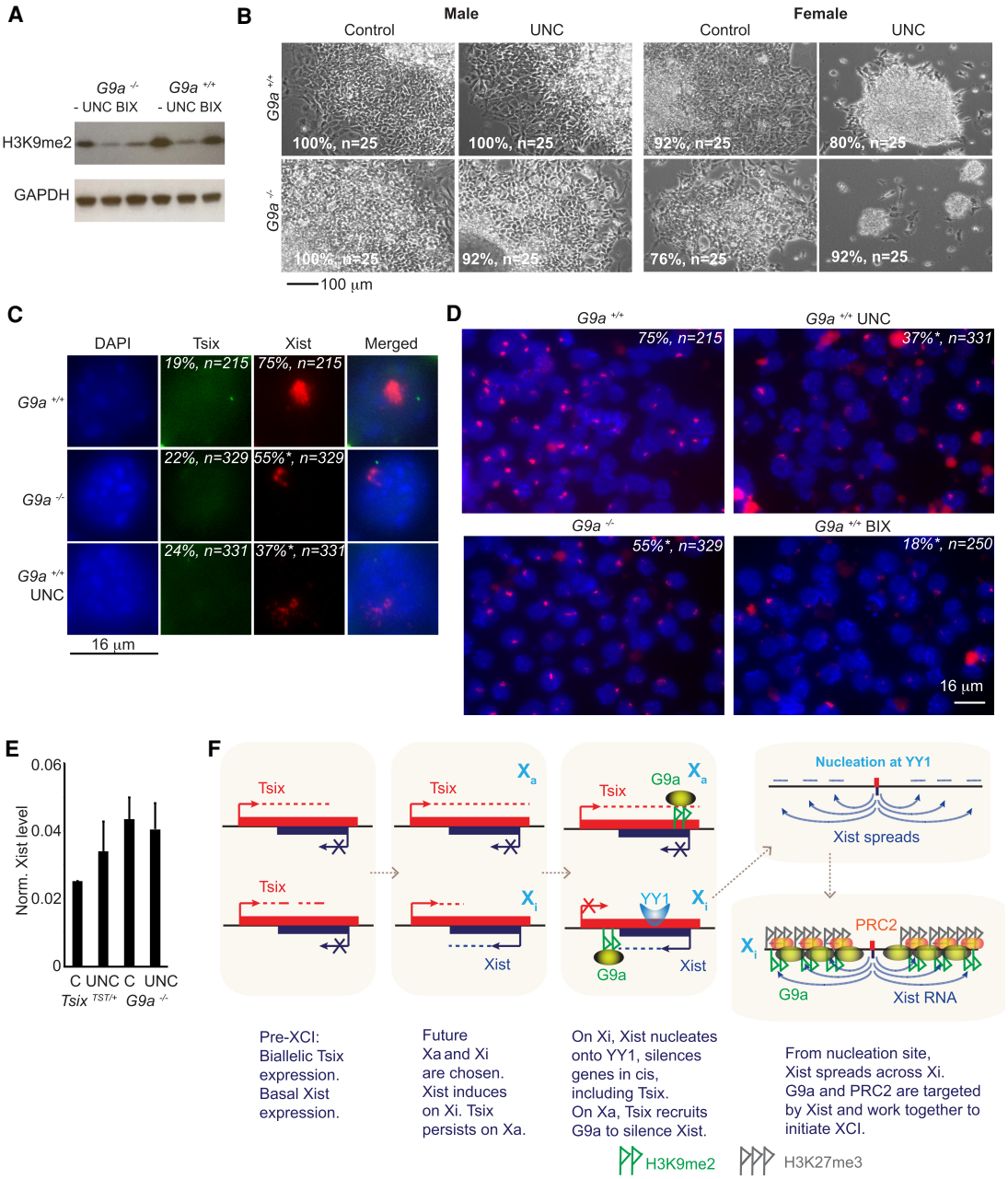

Figure 7. Pharmacological inhibition of H3K9 dimethylation phenocopies G9a deficiency. (*A*) Western blot shows the effect of G9a inhibitors UNC0638 (UNC) and BIX01294 (BIX) on global H3K9me2 level. $G9a^{+/+}$ or $G9a^{-/-}$ ES cells were treated with vehicle DMSO (*C*) or 2 µM inhibitor for 48 h. GAPDH was used as loading control. (*B*) Cells were differentiated for 6 d with LIF withdrawal while treated with vehicle (*C*) or 2 µM UNC. On day 4, EBs were put on gelatinized plates for 2 d to induce outgrow. Representative microscopic images are shown. Percentages of EB (with sample size, *n*) showing the phenotype (either a normal outgrowth or no outgrowth) are indicated in red text for each genotype. See Supplemental Figure S8A for additional examples at various differentiation days. (*C*,*D*) As above, cells were differentiated, and representative images of Xist (*C*,*D*) and Tsix (*C*) RNA-FISH are shown. Nuclei with Xist cloud or with two Tsix spots were counted, and significance was assessed by using χ^2 test. (*) $P < 0.05$. (*E*) RT-qPCR results of normalized Xist expression from cells treated with vehicle or 0.5 µM inhibitor for 7 d. (*F*) Our suggested model how G9a contributes to XCI by inducing H3K9me2 after Xist induction and spreading.

an enrichment of H3K9me2 over gene bodies on the Xi. Given that G9a and PRC2 have been shown to physically interact (Maier et al. 2015; Mozzetta et al. 2015), we propose that G9a and PRC2 may spread together with Xist RNA, potentially in a single large complex, to specifically target H3K9me2 and H3K27me3 to the Xi. Indeed, the H3K9me2 and H3K27me3 marks colocalize with Xist binding sites on the Xi (Fig. 5H; Engreitz et al. 2013; Simon et al. 2013). Our model presents a unified mechanism by which two key repressive marks can be recruited to the

Xi. Notably, repeat A has been shown to interact with other protein factors as well, including the RNA helicase ATRX (Sarma et al. 2014), the megadalton protein SPEN (Chu et al. 2015; McHugh et al. 2015; Minajigi et al. 2015), and RNA methylation protein RBM15 (Patil et al. 2016; Nesterova et al. 2019). We therefore propose that repeat A is an RNA hub for consolidating a large number of XCI factors.

Our study also reconciles previous disagreements over whether H3K9me2 participates in XCI. While early studies suggested that H3K9me2 is an early marker of XCI (Heard et al. 2001; Boggs et al. 2002; Mermoud et al. 2002; Peters et al. 2002), concerns about antibody cross-reactivity with the H3K27me3 mark have been raised (Silva et al. 2003), leading to the notion that Xi genes may be primarily marked by H3K27me3 rather than H3K9me2. In other studies, the role of G9a was tested by creating knockouts in male cells, with one finding no effects on the *Xist* promoter (Rougeulle et al. 2004) and the other finding derepressed genes on the single male X chromosome (Yokochi et al. 2009). Notably, the male background precluded characterization of XCI. In support of the presence of both marks on the Xi, another study showed that CDYL required both H3K27me3 and H3K9me2 to bind the Xi (Escamilla-Del-Arenal et al. 2013). However, a more recent report suggested that knockdown of other H3K9 methyltransferases has little or no effect for the X chromosome in fibroblasts, with the exception of SETDB1 whose depletion did reduce H3K9 methylation (Keniry et al. 2016). Because SETDB1 is predominantly an H3K9 trimethylase, it has been proposed that the H3K9me3 mark may be more relevant for the Xi in fibroblasts (Minkovsky et al. 2014; Keniry et al. 2016). Finally, further uncertainty was created by the observation that neither Xist expression nor maintenance of XCI was affected in G9a-deficient embryos (Ohhata et al. 2004).

In spite of the disparate observations of the past two decades, our present work has the potential to reconcile how G9a and the H3K9me2 can indeed play an important role for gene silencing on the Xi. First, highly specific monoclonal antibodies now enable discrimination among the H3K9me2, H3K9me3, and H3K27me3 marks (Yokochi et al. 2009; Simon et al. 2013; Allis and Jenuwein 2016; Velazquez Camacho et al. 2017; Au Yeung et al. 2019). Second, we investigated function in a female background and could therefore specifically test a role on the Xi. The findings unequivocally establish an enrichment of H3K9me2 marks on the Xi and the functional consequences of losing that mark. Third, in experiments where G9a deficiency was examined in embryos (Ohhata et al. 2004), compensation for the loss of the primary H3K9 dimethylase could very well have occurred during development. There are a number of other H3K9 methyltransferases in mammalian cells, including GLP, SETDB1, SUV39H1, and SUV39H2. Indeed, our present analysis indicates that ablating G9a in ES cells did not fully abolish H3K9me2 (Fig. 1A), suggesting a functional compensation by remaining H3K9 methyltransferases, such as G9a's partner, GLP. In agreement, pharmacological inhibition of both G9a and GLP by a nonselective compound resulted in a much more severe loss of H3K9me2 and more severe recapitulation of the G9a defect in XCI (Fig. 7A–D). Finally, our study focused on the de novo establishment phase of XCI. In several studies where loss of Xi silencing was not observed, the analyses were carried out in post-XCI cells (Minkovsky et al. 2014; Keniry et al. 2016). Present understanding indicates that perturbing XCI is much more difficult during the maintenance phase because of the robust nature of Xi silencing (Brown and Willard 1994; Csankovszki et al. 2001; Minajigi et al. 2015), but is clearly possible if multiple pathways are perturbed for pharmacological X reactivation (Carrette et al. 2018). In summary, our work provides new insight into the role of G9a and H3K9me2, highlights the contribution of noncoding RNA in targeting G9a in *cis*, and integrates valuable studies of the past two decades.

Materials and methods

Cells and differentiation, transfection

Wild-type J1 male and $Tsix^{TST/+}$ female ES cells were described in Lee and Lu (1999) and Ogawa et al. (2008). F1–2.1 female ES cells carrying *rtTA* were a gift from R. Jaenisch (Luikenhuis et al. 2001). Male G9a KO ES cells and their control wild-type male cells were obtained from Prof. Y. Shinkai (Kyoto University) (Tachibana et al. 2005). We used CRISPR technology on $Tsix^{TST/+}$ female ES cells to generate female G9a knockout cells. gRNAs (20mer) were designed using http://crispr.mit.edu (mG9a gRNA v1 sense: caccgGATGGGGGTCGCATCGTGC, mG9a gRNA v2 sense: caccgGCGGGGCCGCATCACTCAT) and cloned into pSpCas9 (BB)-2A-GFP (PX458; a gift from Feng Zhang; Addgene plasmid 48138) (Ran et al. 2013). One day after electroporation of parental $Tsix^{TST/+}$ cells, GFP-positive cells were sorted, and single-cell clones were grown and tested for the deletion. Positive clones were further tested with genomic PCR and sequencing to confirm the microdeletion. Clones were finally tested for ploidity using X chromosome and autosomal DNA-FISH probes. After cloning mouse *G9a* into pBD100 vector with 3× FLAG tag, a stable ES line was generated in F1–2.1 cells after electroporation and selection with 200 µg/mL hygromycin. Single-cell colonies were picked after 10 d of selection and tested for protein expression after inducing with 1 µg/mL doxycycline for 24 h using Western blot. For transient transfection experiments, 293FT cells were used. Twenty-four micrograms of DNA was mixed with 4.8 µL of 200 mM polyethylenimine solution (MW~25 kD) in empty medium, left for 15 min at room temperature, and added to the cells. Transfection efficiency was set to ~80%.

Western blot

Nuclei were isolated after incubating cells in hypotonic buffer (10 mM HEPES at pH 7.9, 1.5 mM $MgCl_2$, 10 mM KCl) for 10 min, and then IGEPAL CA-630 was added at 0.6% final concentration, vortexed, and spun for 1 min at max speed. Nuclei were suspended in high-salt buffer (20 mM HEPES at pH 7.9, 1.5 mM $MgCl_2$, 25% glycerol, 2.5 M NaCl, 0.05% IGEPAL CA-630 and protease inhibitors). After rotating for 30 min at 4°C, debris was removed by spinning at max speed for 15 min. Salt concentration was set to 150 mM before SDS-PAGE. For CLIP Western, the membrane was first exposed for autoradiography and then blocked, and antibodies were added as normally into 5% dray fat milk in PBS + 0.5% Tween-20. Anti-G9a antibody (R&D clone A8620A), anti-

H3K9me2 (Abcam ab1220), anti-Oct-3/4 (Santa Cruz H134), or anti-FLAG (Sigma M2) was used for Western analysis.

Quantitative RT-PCRRNA was isolated from 1×10^7 to 2×10^7 cells with Qiagen RNeasy kit and DNase-treated, and 100 ng of total RNA/reaction was reverse-transcribed using SuperScript III and gene-specific reverse primers following the manufacturer's instructions. For quantitative PCR cDNA or diluted ChIP, DNA was used with Bio-Rad iQ SYBR Green Supermix and custom-designed primers listed in Supplemental Table S1. Relative quantitation was performed in a CFX96 Bio-Rad system using Δ-ΔCt method and cyclophilin A, Gapdh, or α-tubulin as a housekeeping control. In case of ChIP, DNA input was used for normalization. All reactions were run in triplicates, and Student's *t*-test was used to calculate significance comparing biological replicates ($n \geq 3$).

UV cross-linking and RNA immunoprecipitation

UV-RIP was performed as described previously (Ule et al. 2003; Jensen and Darnell 2008) with modifications indicated below. After being trypsinized and washed in PBS, 1.3×10^7 cells were cross-linked using Stratalinker 1800 UV irradiation at 256 nm for 250 mJ/cm^2. Cell pellets were kept at −80°C. For each immunoprecipitation (IP), cell pellets were resuspended in 1 mL hypotonic buffer (10 mM HEPES at pH 7.9, 1.5 mM $MgCl_2$, 10 mM KCl, 1 mM AEBSF, protease inhibitor cocktail, and RNase inhibitor) and incubated for 15 min on ice. Next, 1% digitonin and 0.1% Triton X-100 was added, and cells were suspended five times with a 1-mL pipette. Nuclei were pelleted at 2500*g* for 5 min, washed in 1 mL hypotonic buffer, and resuspended in 1 mL of IP buffer (PBS supplemented with extra 150 mM NaCl, 10% glycerol, 0.5% Triton X-100, 1 mM AEBSF, protease, RNase inhibitors) and incubated for 10 min on ice. After adding 40 U of TurboDNase and 2 mM $CaCl_2$, lysates were incubated for 30 min at 37°C rotating. Next, we added 5 mM EDTA, an extra 150 mM NaCl (450 mM final), and 0.5% laurylsarcosine. After rotating for 30 min at 4°C, cell debris was pelleted at 16,000*g* for 15 min, and the lysate was diluted again with 1 vol of IP dilution buffer (20 mM HEPES, 0.5% Triton-X100). Five percent was removed and saved as input for RNA extraction. Lysate was split into two aliquots and immunoprecipitated overnight with IgG-negative control or anti-G9a antibody. Magnetic protein G beads were added after overnight IP for 1 h. Beads were washed as follows: three times with high-salt wash buffer (10 mM Tris-HCl at pH 7.5, 500 mM NaCl, 0.1% SDS, 0.5% sodium deoxycholate, 0.5% Nonidet-P40) and twice with low-salt buffer (10 mM Tris-HCl at pH 7.5, 1% Nonidet-P40). RNA was eluted by incubation in prewarmed proteinase K buffer (100 mM Tris-HCl at pH 7.5, 50 mM NaCl, 10 mM EDTA, 0.5% SDS, 20 mg/mL proteinase K) for 30 min at 37°C with frequent vortexing. RNA was then phenol-extracted from the supernatant. RNA was analyzed by quantitative RT-PCR.

RNA sequencing

Total RNA was isolated and DNase-treated as for RT-PCR. After rRNA subtraction with an Epicentre Ribo-Zero kit, Illumina libraries were generated using NEBNext Ultra directional RNA library preparation set (New England Biolabs) following the manufacturer's instructions and submitted for Illumina deep sequencing.

Chromatin immunoprecipitation (ChIP)

Cells (1.3×10^7) were fixed in 1% formaldehyde for 6 min at room temperature. Glycine (125 mM) was added, and cells were harvested, washed in PBS, and kept at −80°C. For chromatin isolated pellet was suspended in 1 mL of buffer 1 (50 mM HEPES at pH 7.5, 150 mM NaCl, 1 mM EDTA, 0.5% IGECAP CA-630, 0.25% Triton X-100, protease inhibitors). After rotating for 10 min at 4°C, nuclei were collected by spinning at 1700*g* for 5 min and then suspended in buffer 2 (10 mM Tris-HCl at pH 8, 200 mM NaCl, 5 mM EDTA, 2.5 mM EGTA, protease inhibitors). After another 10-min rotation at 4°C and spinning at 1700*g* for 5 min, nuclei were suspended in buffer 3 (10 mM Tris-HCl at pH 8, 5 mM EDTA, 2.5 mM EGTA, protease inhibitors). RNase A (20 mg/mL) and 0.5% lauroyl-sarcosine were added and rotated for 30 min at 37°C. Next, chromatin was sheared using Diagenode Bioruptor XL twice for 20 min each (with 30 sec on, 30 sec off cycles). Debris was separated by spinning at 15,000*g* for 15 min. Supernatant was diluted 1:2 with dilution buffer (30 mM Tris-HCl at pH 8, 300 mM NaCl, 2% Triton X-100). Input was removed, and 2 µg of antibodies was added to the lysate, respectively: negative control IgG, anti-G9a (R&D clone A8620A), anti-H3K9me2 (Abcam ab1220), or anti-H3K9Ac (Abcam ab4441). After overnight immunoprecipitation, magnetic protein G was added for 1 h, and then beads were washed five times with wash buffer (50 mM HEPES at pH 7.5, 10 mM EDTA, 0.5% sodium-deoxycholate, 1% IGEPAL CA-630, 0.5 M NaCl) and once with TEN (10 mM Tris-HCl at pH 8, 50 mM NaCl, 1 mM EDTA). Next, ChIP material was eluted by suspending beads in TES (50 mM Tris-HCl at pH 8, 1% SDS, 10 mM EDTA) and incubated for 20 min at 65°C with frequent vortexing. Cross-links were reversed overnight at 65°C while adding 40 µg of proteinase K. DNA was isolated by phenol extraction and ethanol precipitation and used for Q-PCR or library construction with New England Biolabs' NebNext ChIP-seq library preparation master mix and following the manufacturer's instructions.

Protein purification

Mouse G9a cDNA was cloned into pFASTBAC1 with 3× FLAG tag. Protein was isolated from infected Sf9 cell pellets using magnetic anti-FLAG M2 beads. After washing beads twice with high-salt PBS supplemented with 750 mM NaCl and 0.5% Triton X-100, protein was eluted with 3× FLAG peptide. Protein was finally concentrated on Amicon 100-kD size exclusion columns. GFP-FLAG and GST-His were expressed in BL21 *E. coli* and purified using magnetic anti-FLAG M2 (Sigma-Aldrich) or glutathion-sepharose beads (GE Healthcare Life Sciences), respectively, following the manufacturers' instructions.

In vitro RNA-binding assays

cDNAs of RNA fragments were cloned into pcDNA3 or pGEM7 vectors. After linearizing the vectors, RNA or amplified by PCR was in vitro transcribed using either AmpliScribe T7 high-yield transcription kit (Epicentre) or SP6 Megascript transcription kit (Life Technologies) following the manufacturers' instructions. For RNA EMSA, 20 pmol RNA was labeled with [©-^{32}P]-ATP using T4 polynucleotide kinase and purified on G50 columns. Labeled RNA (0.3–2 kcpm) was folded first by denaturing in 300 mM NaCl at 95°C and then kept at 37°C followed by 10 min at room temperature. Next, 10 mM HEPES (pH 8) and 10 mM $MgCl_2$ was added and kept on ice. For in vitro binding, 150–500 nM protein was incubated with folded RNAs at room temperature in binding buffer (20 mM HEPES at pH 8, 150 mM NaCl, 1.5 mM $MgCl_2$, 1 mM DTT, 0.01 ìg/ìl BSA, 0.005% IGEPAL CA-630, 5% glycerol, 25 ng/ìl yeast tRNA). For competition assay, 10 pM radioactive RNA was mixed with 2× folding buffer (600 mM NaCl, 10 mM MgCl2, 20 mM Tris 1M at pH 8.0, 2

mM EDTA). RNA was folded by heating to 2 min at 95°C and cooling down to 4°C at a 0.1°C/sec rate. G9a and GFP (1, 2, 4, 10, 20, 40, and 100 nM) were incubated with folded RNA and 20 nM Ezh2 in 4× RNA-binding buffer (200 mM Tris HCl at pH 8, 400 mM NaCl, 20 mM MgCl2, 4 mM DTT, 20% glycerol, 0.2% NP40, 8 U/µL RNase out) for 30 min at 30°C. After incubation for RNA EMSA, the RNA–protein complexes were resolved in 0.4% agarose gel and 1× THEM running buffer (66 mM HEPES, 34 mM Tris-HCl at pH 7.4, 1 mM EDTA, 10 mM $MgCl_2$). Autoradiography was done by exposing the dried gel onto a phosphoscreen and scanned on Typhoon phosphorimager (GE Healthcare Life Sciences). For in vitro binding assay, anti-FLAG beads were added to the binding reaction for 30 min, and beads were washed five times with high-salt PBS (300 mM final NaCl, 0.5% IGEPAL CA-630) and RNA was isolated by phenol extraction and ethanol precipitation. RNA was then quantified with quantitative RT-PCR.

Histone methyltransferase assay

Methyltransferase assay was performed as earlier (Cifuentes-Rojas et al. 2014). Briefly, 5S nucleosomal arrays were assembled with purified *E. coli* expressed core histones. HMTase reactions were assembled in methylation buffer (50 mM Tris-HCl at pH 8.5, 5 mM $MgCl_2$, 4mM DTT) containing nucleosomes, 0.33 mM [^{3}H]-S-adenosyl-methionine (Perkin Elmer), the indicated [RNA], PRC2, and incubated at 30°C. Fixed-time assays were incubated for 60 min, while for kinetic assays, aliquots (15 µL for reactions with 150 nM PRC2, 30 µL for reactions with 20 nM PRC2) were removed at the indicated times and quenched with Laemmli buffer, resolved by 18% SDS-PAGE, and transferred to an Immobilon-P membrane (Millipore). Blots were Coomassie-stained, sprayed with EN^{3}HANCE (Perkin Elmer), and exposed to film.

Immunostaining and RNA-FISH

Experiments were performed as described (Lee and Lu 1999; Zhang et al. 2007). Xist and Tsix RNA were detected using Cy3-labeled Xist and 6FAM-labeled Tsix oligo probe cocktails. After 4 h of incubation, slides were washed three times with 30% formamide, 2× SSC, and 3× with 2× SSC at room temperature and then rinsed once with PBS + 0.2% Tween-20. For immunostaining, after blocking with 2% BSA in PBS for 15 min at room temperature, the primary antibodies anti-G9a (R&D clone A8620A) or anti-H3K9me2 (Abcam ab1220) were added and washed similarly to above. Digital images were taken with a Nikon Eclipse 90i microscope (Nikon Instruments, Inc.) and processed using Volocity software (Improvision). Cells were counted and scored for the presence or absence of an Xist RNA cloud or checked for ploidity.

Bioinformatics

All libraries were sequenced with Illumina HiSeq 2000 using 50 cycles to obtain paired-end reads. For non-allele-specific analysis, adaptor-trimmed reads were aligned to mm9 reference genome, while for allele-specific analysis to custom *mus*/129 and *cas* genomes, the aligned reads were lifted over to reference mm9 genome (Pinter et al. 2012). RNA was aligned with TopHat (Trapnell et al. 2012) and ChIP DNA with Novoalign. For RNA analysis, transcripts were assembled strand-specifically with Homer (Heinz et al. 2010), and tag libraries were generated over coding regions using the condensed genes option using Homer's built in mm9 reference genome. Nonuniquely aligned reads and PCR duplicates were excluded. Differentially expressed genes were called between day 0 and day 10, $Tsix^{TST/+}$ (i.e., $G9a^{+/+}$) and $G9a^{-/-}$ cells based on fold change (min. 1.5-fold) and significance ($P < 0.05$) in three biological replicates. Gene subsets based on expression levels were sorted by RPKM values of the control cells at day 0 or day 10. For allelic analysis, we calculated allelic skew (AS) by taking the number of allele-specifically aligned reads over the genes: (cas − mus)/(cas + mus). Allele-specifically expressed genes were called significantly biased after running a negative binominal distribution analysis with minimum 10 reads per gene and $P < 0.05$. To compare AS between paired samples, Student's *t*-test or Wilcoxon test was used as indicated or to assess overall chromosome-wide differences, Mann–Whitney test was used. χ^2 test was used to test significance in the number of genes being affected in control or knockout.

Pathway analysis was performed using overrepresentation analysis method of WebGestalt (web-based gene set analysis toolkit; http://www.webgestalt.org). Significantly overrepresented pathways were used ($P < 0.05$, FDR < 0.05).

ChIP-seq samples from the two biological replicates were compared by calculating coverage over 100-kb windows, scatter plots were generated in R/ggplot, and R^2 values were calculated. When merging the two data sets, an equal number of reads were randomly sampled from each corresponding condition after alignment, and input normalization was performed with deepTools/bamCompare after PCR duplicate removal, filtering out three blacklist regions (chr2: 98502146–98507766, chr9: 2999324–3039266, and chr9: 35112681–35113357) and fragments >1000 nt in size, producing read-centered, 50-nt binned, 300-nt smoothed data sets. Metagene profiles and heat maps were generated with deepTools (Ramírez et al. 2016). We also called peaks with macs2 (Zhang et al. 2008) compared with input ($q < 0.05$ and 0.05 broad cutoff). Called peaks were then mapped onto genes or gene body + 3kb 5′ upstream regions using the bedtools map, and genes were further analyzed. H3K9Ac and H3K9me2 genome-wide coverages were compared by randomly sampling equal numbers of samples from the conditions, and after removing repeats and duplicates, artifact read pile-up regions using blacklisting violin plots were generated on $\log_2$-normalized coverages over the gene bodies for H3K9me2 or over the macs2-called peaks ($P < 0.0005$) for H3K9Ac. To calculate significance, Wilcoxon test was used. ChIP CDPs were used to plot allelic ratio (mus/mus + cas) in controls and knockouts.

ChIP sequencing data were aligned allele-specifically as above, and unique, nonrepeat reads were assigned as mus- or cas-specific based on the available SNPs or as neutral if no SNP information was available or the coverage was similar on both alleles. Composite (comp) tracks contained all of the above three types of reads. Reference genes were defined based on Ensembl NCBIM67 (Ensembl release 67). Allelic skew (AS) was calculated by normalized allele-specific coverages. Mus-specific allelic skew values were used to compare knockout values with controls, and Wilcoxon test was used to calculate significance. Cumulative binomial distribution probability ($P < 0.05$) was used to obtain genes with significant allelic bias on the histone marks, and similarly to above, control and knockout samples were compared using Wilcoxon test. Genes with at least twofold difference or no change between $Tsix^{TST/+}$ and $G9a^{-/-}$ coverage were sorted to compare allelic skew changes, and allele-specific metagene profiles were looked at specifically on these regions on chrX using deepTools. Allelic skew (AS) was calculated for H3K9me2 and H3K9Ac similarly as for RNA expression, and changes in AS was compared between $Tsix^{TST/+}$ and $G9a^{-/-}$ cells especially on distinctly methylated or acetylated regions. Next, differently methylated genes were compared with differently acetylated promoters and also with RNA expression data. Finally, G9a-dependent

H3K9me2-ed genes were compared across chrX and Xist binding sites from Simon et al. (2013) using 1-Mb windows, and the Pearson correlation coefficient was calculated. Both RNA-seq and ChIP-seq data have been deposited to GEO under GSE130057 study.

Competing interest statement

J.T.L. is a cofounder of Translate Bio and Fulcrum Therapeutics and serves as Advisor to Skyhawk Therapeutics. A.S. is currently a full-time employee and shareholder of Epizyme, Inc.

Acknowledgments

We are grateful to Prof. Y. Shinkai (Kyoto University) for providing us with male *G9a*$^{-/-}$ and control ES cells and G9a expression vector. We thank all laboratory members for helpful advice and many important discussions. This work was funded by grants from the National Institutes of Health (R01-HD097665) and the Howard Hughes Medical Institute to J.T.L.

Author contributions: A.S. and J.T.L. conceived of the project and wrote the paper. A.S. performed experiments and bioinformatics analysis. R.A. contributed to RNA-EMSA and ChIP experiments. D.W. performed GFP competition EMSAs. B.K. and R.B. performed bioinformatics analysis. B.C.d.R. provided pBD100 vector for inducible G9a expression and purified GST and GFP-FLAG proteins. C.C.-R. helped to design and perform the in vitro biochemical assays and with protein expression. K.K.-T. assisted with experiments and generated stable cell lines and libraries for sequencing. All authors significantly contributed to experimental design, troubleshooting, and critical evaluation of the results.

References

Allis CD, Jenuwein T. 2016. The molecular hallmarks of epigenetic control. *Nat Rev Genet* **17:** 487–500. doi:10.1038/nrg.2016.59

Almeida M, Pintacuda G, Masui O, Koseki Y, Gdula M, Cerase A, Brown D, Mould A, Innocent C, Nakayama M, et al. 2017. PCGF3/5-PRC1 initiates Polycomb recruitment in X chromosome inactivation. *Science* **356:** 1081–1084. doi:10.1126/science.aal2512

Au Yeung WK, Brind'Amour J, Hatano Y, Yamagata K, Feil R, Lorincz MC, Tachibana M, Shinkai Y, Sasaki H. 2019. Histone H3K9 methyltransferase G9a in oocytes is essential for preimplantation development but dispensable for CG methylation protection. *Cell Rep* **27:** 282–293.e4. doi:10.1016/j.celrep.2019.03.002

Beard C, Li E, Jaenisch R. 1995. Loss of methylation activates Xist in somatic but not in embryonic cells. *Genes Dev* **9:** 2325–2334. doi:10.1101/gad.9.19.2325

Blewitt ME, Gendrel AV, Pang Z, Sparrow DB, Whitelaw N, Craig JM, Apedaile A, Hilton DJ, Dunwoodie SL, Brockdorff N, et al. 2008. SmcHD1, containing a structural-maintenance-of-chromosomes hinge domain, has a critical role in X inactivation. *Nat Genet* **40:** 663–669. doi:10.1038/ng.142

Boggs BA, Cheung P, Heard E, Spector DL, Chinault AC, Allis CD. 2002. Differentially methylated forms of histone H3 show unique association patterns with inactive human X chromosomes. *Nat Genet* **30:** 73–76. doi:10.1038/ng787

Brockdorff N, Ashworth A, Kay GF, McCabe VM, Norris DP, Cooper PJ, Swift S, Rastan S. 1992. The product of the mouse Xist gene is a 15 kb inactive X-specific transcript containing no conserved ORF and located in the nucleus. *Cell* **71:** 515–526. doi:10.1016/0092-8674(92)90519-I

Brown CJ, Willard HF. 1994. The human X-inactivation centre is not required for maintenance of X-chromosome inactivation. *Nature* **368:** 154–156. doi:10.1038/368154a0

Brown CJ, Hendrich BD, Rupert JL, Lafrenière RG, Xing Y, Lawrence J, Willard HF. 1992. The human XIST gene: analysis of a 17 kb inactive X-specific RNA that contains conserved repeats and is highly localized within the nucleus. *Cell* **71:** 527–542. doi:10.1016/0092-8674(92)90520-M

Carrette LLG, Wang CY, Wei C, Press W, Ma W, Kelleher RJ 3rd, Lee JT. 2018. A mixed modality approach towards Xi reactivation for Rett syndrome and other X-linked disorders. *Proc Natl Acad Sci* **115:** E668–E675. doi:10.1073/pnas.1715124115

Chu C, Zhang QC, da Rocha ST, Flynn RA, Bharadwaj M, Calabrese JM, Magnuson T, Heard E, Chang HY. 2015. Systematic discovery of Xist RNA binding proteins. *Cell* **161:** 404–416. doi:10.1016/j.cell.2015.03.025

Cifuentes-Rojas C, Hernandez AJ, Sarma K, Lee JT. 2014. Regulatory interactions between RNA and polycomb repressive complex 2. *Mol Cell* **55:** 171–185. doi:10.1016/j.molcel.2014.05.009

Clemson CM, McNeil JA, Willard HF, Lawrence JB. 1996. XIST RNA paints the inactive X chromosome at interphase: evidence for a novel RNA involved in nuclear/chromosome structure. *J Cell Biol* **132:** 259–275. doi:10.1083/jcb.132.3.259

Colognori D, Sunwoo H, Kriz AJ, Wang CY, Lee JT. 2019. Xist deletional analysis reveals an interdependency between Xist RNA and Polycomb complexes for spreading along the inactive X. *Mol Cell* **74:** 101–117.e10. doi:10.1016/j.molcel.2019.01.015

Csankovszki G, Nagy A, Jaenisch R. 2001. Synergism of Xist RNA, DNA methylation, and histone hypoacetylation in maintaining X chromosome inactivation. *J Cell Biol* **153:** 773–784. doi:10.1083/jcb.153.4.773

Davidovich C, Wang X, Cifuentes-Rojas C, Goodrich KJ, Gooding AR, Lee JT, Cech TR. 2015. Toward a consensus on the binding specificity and promiscuity of PRC2 for RNA. *Mol Cell* **57:** 552–558. doi:10.1016/j.molcel.2014.12.017

Disteche CM. 2012. Dosage compensation of the sex chromosomes. *Annu Rev Genet* **46:** 537–560. doi:10.1146/annurev-genet-110711-155454

Dupont C, Gribnau J. 2013. Different flavors of X-chromosome inactivation in mammals. *Curr Opin Cell Biol* **25:** 314–321. doi:10.1016/j.ceb.2013.03.001

Engreitz JM, Pandya-Jones A, McDonel P, Shishkin A, Sirokman K, Surka C, Kadri S, Xing J, Goren A, Lander ES, et al. 2013. The Xist lncRNA exploits three-dimensional genome architecture to spread across the X chromosome. *Science* **341:** 1237973. doi:10.1126/science.1237973

Escamilla-Del-Arenal M, da Rocha ST, Spruijt CG, Masui O, Renaud O, Smits AH, Margueron R, Vermeulen M, Heard E. 2013. Cdyl, a new partner of the inactive X chromosome and potential reader of H3K27me3 and H3K9me2. *Mol Cell Biol* **33:** 5005–5020. doi:10.1128/MCB.00866-13

Feldman N, Gerson A, Fang J, Li E, Zhang Y, Shinkai Y, Cedar H, Bergman Y. 2006. G9a-mediated irreversible epigenetic inactivation of Oct-3/4 during early embryogenesis. *Nat Cell Biol* **8:** 188–194. doi:10.1038/ncb1353

Gendrel AV, Apedaile A, Coker H, Termanis A, Zvetkova I, Godwin J, Tang YA, Huntley D, Montana G, Taylor S, et al. 2012. Smchd1-dependent and -independent pathways determine developmental dynamics of CpG island methylation on the inactive X chromosome. *Dev Cell* **23:** 265–279. doi:10.1016/j.devcel.2012.06.011

Guler GD, Tindell CA, Pitti R, Wilson C, Nichols K, KaiWai Cheung T, Kim HJ, Wongchenko M, Yan Y, Haley B, et al. 2017. Repression of stress-induced LINE-1 expression protects cancer cell subpopulations from lethal drug exposure. *Cancer Cell* **32:** 221–237.e13. doi:10.1016/j.ccell.2017.07.002

Heard E, Rougeulle C, Arnaud D, Avner P, Allis CD, Spector DL. 2001. Methylation of histone H3 at Lys-9 is an early mark on the X chromosome during X inactivation. *Cell* **107:** 727–738. doi:10.1016/S0092-8674(01)00598-0

Heinz S, Benner C, Spann N, Bertolino E, Lin YC, Laslo P, Cheng JX, Murre C, Singh H, Glass CK. 2010. Simple combinations of lineage-determining transcription factors prime cis-regulatory elements required for macrophage and B cell identities. *Mol Cell* **38:** 576–589. doi:10.1016/j.molcel.2010.05.004

Jégu T, Aeby E, Lee JT. 2017. The X chromosome in space. *Nat Rev Genet* **18:** 377–389. doi:10.1038/nrg.2017.17

Jégu T, Blum R, Cochrane JC, Yang L, Wang CY, Gilles ME, Colognori D, Szanto A, Marr SK, Kingston RE, et al. 2019. Xist RNA antagonizes the SWI/SNF chromatin remodeler BRG1 on the inactive X chromosome. *Nat Struct Mol Biol* **26:** 96–109. doi:10.1038/s41594-018-0176-8

Jensen KB, Darnell RB. 2008. CLIP: crosslinking and immunoprecipitation of in vivo RNA targets of RNA-binding proteins. *Methods Mol Biol* **488:** 85–98. doi:10.1007/978-1-60327-475-3_6

Jeon Y, Lee JT. 2011. YY1 tethers Xist RNA to the inactive X nucleation center. *Cell* **146:** 119–133. doi:10.1016/j.cell.2011.06.026

Keniry A, Gearing LJ, Jansz N, Liu J, Holik AZ, Hickey PF, Kinkel SA, Moore DL, Breslin K, Chen K, et al. 2016. Setdb1-mediated H3K9 methylation is enriched on the inactive X and plays a role in its epigenetic silencing. *Epigenetics Chromatin* **9:** 16. doi:10.1186/s13072-016-0064-6

Kohlmaier A, Savarese F, Lachner M, Martens J, Jenuwein T, Wutz A. 2004. A chromosomal memory triggered by Xist regulates histone methylation in X inactivation. *PLoS Biol* **2:** E171. doi:10.1371/journal.pbio.0020171

Kubicek S, O'Sullivan RJ, August EM, Hickey ER, Zhang Q, Teodoro ML, Rea S, Mechtler K, Kowalski JA, Homon CA, et al. 2007. Reversal of H3K9me2 by a small-molecule inhibitor for the G9a histone methyltransferase. *Mol Cell* **25:** 473–481. doi:10.1016/j.molcel.2007.01.017

Lee JT. 2012. Epigenetic regulation by long noncoding RNAs. *Science* **338:** 1435–1439. doi:10.1126/science.1231776

Lee JT, Lu N. 1999. Targeted mutagenesis of *Tsix* leads to nonrandom X inactivation. *Cell* **99:** 47–57. doi:10.1016/S0092-8674(00)80061-6

Lee JT, Davidow LS, Warshawsky D. 1999. *Tsix*, a gene antisense to *Xist* at the X-inactivation centre. *Nat Genet* **21:** 400–404. doi:10.1038/7734

Luikenhuis S, Wutz A, Jaenisch R. 2001. Antisense transcription through the *Xist* locus mediates *Tsix* function in embryonic stem cells. *Mol Cell Biol* **21:** 8512–8520. doi:10.1128/MCB.21.24.8512-8520.2001

Maier VK, Feeney CM, Taylor JE, Creech AL, Qiao JW, Szanto A, Das PP, Chevrier N, Cifuentes-Rojas C, Orkin SH, et al. 2015. Functional proteomic analysis of repressive histone methyltransferase complexes reveals ZNF518B as a G9A regulator. *Mol Cell Proteomics* **14:** 1435–1446. doi:10.1074/mcp.M114.044586

McHugh CA, Chen CK, Chow A, Surka CF, Tran C, McDonel P, Pandya-Jones A, Blanco M, Burghard C, Moradian A, et al. 2015. The Xist lncRNA interacts directly with SHARP to silence transcription through HDAC3. *Nature* **521:** 232–236. doi:10.1038/nature14443

Melé M, Rinn JL. 2016. 'Cat's cradling' the 3D genome by the act of lncRNA transcription. *Mol Cell* **62:** 657–664. doi:10.1016/j.molcel.2016.05.011

Mermoud JE, Popova B, Peters AH, Jenuwein T, Brockdorff N. 2002. Histone H3 lysine 9 methylation occurs rapidly at the onset of random X chromosome inactivation. *Curr Biol* **12:** 247–251. doi:10.1016/S0960-9822(02)00660-7

Minajigi A, Froberg J, Wei C, Sunwoo H, Kesner B, Colognori D, Lessing D, Payer B, Boukhali M, Haas W, et al. 2015. Chromosomes. A comprehensive Xist interactome reveals cohesin repulsion and an RNA-directed chromosome conformation. *Science* **349:** aab2276. doi:10.1126/science.aab2276

Minkovsky A, Sahakyan A, Rankin-Gee E, Bonora G, Patel S, Plath K. 2014. The Mbd1-Atf7ip-Setdb1 pathway contributes to the maintenance of X chromosome inactivation. *Epigenetics Chromatin* **7:** 12. doi:10.1186/1756-8935-7-12

Moindrot B, Cerase A, Coker H, Masui O, Grijzenhout A, Pintacuda G, Schermelleh L, Nesterova TB, Brockdorff N. 2015. A pooled shRNA screen identifies Rbm15, Spen, and Wtap as factors required for Xist RNA-mediated silencing. *Cell Rep* **12:** 562–572. doi:10.1016/j.celrep.2015.06.053

Monfort A, Di Minin G, Postlmayr A, Freimann R, Arieti F, Thore S, Wutz A. 2015. Identification of *Spen* as a crucial factor for *Xist* function through forward genetic screening in haploid embryonic stem cells. *Cell Rep* **12:** 554–561. doi:10.1016/j.celrep.2015.06.067

Morey C, Navarro P, Debrand E, Avner P, Rougeulle C, Clerc P. 2004. The region 3′ to Xist mediates X chromosome counting and H3 Lys-4 dimethylation within the Xist gene. *EMBO J* **23:** 594–604. doi:10.1038/sj.emboj.7600071

Mozzetta C, Pontis J, Fritsch L, Robin P, Portoso M, Proux C, Margueron R, Ait-Si-Ali S. 2014. The histone H3 lysine 9 methyltransferases G9a and GLP regulate polycomb repressive complex 2-mediated gene silencing. *Mol Cell* **53:** 277–289. doi:10.1016/j.molcel.2013.12.005

Mozzetta C, Pontis J, Ait-Si-Ali S. 2015. Functional crosstalk between lysine methyltransferases on histone substrates: the case of G9A/GLP and Polycomb repressive complex 2. *Antioxid Redox Signal* **22:** 1365–1381. doi:10.1089/ars.2014.6116

Nagano T, Mitchell JA, Sanz LA, Pauler FM, Ferguson-Smith AC, Feil R, Fraser P. 2008. The Air noncoding RNA epigenetically silences transcription by targeting G9a to chromatin. *Science* **322:** 1717–1720. doi:10.1126/science.1163802

Nesterova TB, Wei G, Coker H, Pintacuda G, Bowness JS, Zhang T, Almeida M, Bloechl B, Moindrot B, Carter EJ, et al. 2019. Systematic allelic analysis defines the interplay of key pathways in X chromosome inactivation. *Nat Commun* **10:** 3129. doi:10.1038/s41467-019-11171-3

Ogawa Y, Lee JT. 2003. Xite, X-inactivation intergenic transcription elements that regulate the probability of choice. *Mol Cell* **11:** 731–743. doi:10.1016/S1097-2765(03)00063-7

Ogawa Y, Sun BK, Lee JT. 2008. Intersection of the RNA interference and X-inactivation pathways. *Science* **320:** 1336–1341. doi:10.1126/science.1157676

Ohhata T, Tachibana M, Tada M, Tada T, Sasaki H, Shinkai Y, Sado T. 2004. X-inactivation is stably maintained in mouse embryos deficient for histone methyl transferase G9a. *Genesis* **40:** 151–156. doi:10.1002/gene.20077

Ohhata T, Hoki Y, Sasaki H, Sado T. 2008. Crucial role of antisense transcription across the *Xist* promoter in *Tsix*-mediated *Xist* chromatin modification. *Development* **135:** 227–235. doi:10.1242/dev.008490

Pandey RR, Mondal T, Mohammad F, Enroth S, Redrup L, Komorowski J, Nagano T, Mancini-Dinardo D, Kanduri C. 2008. Kcnq1ot1 antisense noncoding RNA mediates lineage-

specific transcriptional silencing through chromatin-level regulation. *Mol Cell* **32:** 232–246. doi:10.1016/j.molcel.2008.08.022

Patil DP, Chen CK, Pickering BF, Chow A, Jackson C, Guttman M, Jaffrey SR. 2016. M^6A RNA methylation promotes *XIST*-mediated transcriptional repression. *Nature* **537:** 369–373. doi:10.1038/nature19342

Peters AH, Mermoud JE, O'Carroll D, Pagani M, Schweizer D, Brockdorff N, Jenuwein T. 2002. Histone H3 lysine 9 methylation is an epigenetic imprint of facultative heterochromatin. *Nat Genet* **30:** 77–80. doi:10.1038/ng789

Peters AH, Kubicek S, Mechtler K, O'Sullivan RJ, Derijck AA, Perez-Burgos L, Kohlmaier A, Opravil S, Tachibana M, Shinkai Y, et al. 2003. Partitioning and plasticity of repressive histone methylation states in mammalian chromatin. *Mol Cell* **12:** 1577–1589. doi:10.1016/S1097-2765(03)00477-5

Pinter SF, Sadreyev RI, Yildirim E, Jeon Y, Ohsumi TK, Borowsky M, Lee JT. 2012. Spreading of X chromosome inactivation via a hierarchy of defined Polycomb stations. *Genome Res* **22:** 1864–1876. doi:10.1101/gr.133751.111

Plath K, Fang J, Mlynarczyk-Evans SK, Cao R, Worringer KA, Wang H, de la Cruz CC, Otte AP, Panning B, Zhang Y. 2003. Role of histone H3 lysine 27 methylation in X inactivation. *Science* **300:** 131–135. doi:10.1126/science.1084274

Ramírez F, Ryan DP, Grüning B, Bhardwaj V, Kilpert F, Richter AS, Heyne S, Dündar F, Manke T. 2016. Deeptools2: a next generation web server for deep-sequencing data analysis. *Nucleic Acids Res* **44:** W160–W165. doi:10.1093/nar/gkw257

Ran FA, Hsu PD, Wright J, Agarwala V, Scott DA, Zhang F. 2013. Genome engineering using the CRISPR-Cas9 system. *Nat Protoc* **8:** 2281–2308. doi:10.1038/nprot.2013.143

Rice JC, Briggs SD, Ueberheide B, Barber CM, Shabanowitz J, Hunt DF, Shinkai Y, Allis CD. 2003. Histone methyltransferases direct different degrees of methylation to define distinct chromatin domains. *Mol Cell* **12:** 1591–1598. doi:10.1016/S1097-2765(03)00479-9

Rougeulle C, Chaumeil J, Sarma K, Allis CD, Reinberg D, Avner P, Heard E. 2004. Differential histone H3 Lys-9 and Lys-27 methylation profiles on the X chromosome. *Mol Cell Biol* **24:** 5475–5484. doi:10.1128/MCB.24.12.5475-5484.2004

Sado T, Wang Z, Sasaki H, Li E. 2001. Regulation of imprinted X-chromosome inactivation in mice by Tsix. *Development* **128:** 1275–1286. doi:10.1242/dev.128.8.1275

Sado T, Hoki Y, Sasaki H. 2005. *Tsix* silences *Xist* through modification of chromatin structure. *Dev Cell* **9:** 159–165. doi:10.1016/j.devcel.2005.05.015

Sarma K, Levasseur P, Aristarkhov A, Lee JT. 2010. Locked nucleic acids (LNAs) reveal sequence requirements and kinetics of Xist RNA localization to the X chromosome. *Proc Natl Acad Sci* **107:** 22196–22201. doi:10.1073/pnas.1009785107

Sarma K, Cifuentes-Rojas C, Ergun A, Del Rosario A, Jeon Y, White F, Sadreyev R, Lee JT. 2014. ATRX directs binding of PRC2 to Xist RNA and Polycomb targets. *Cell* **159:** 869–883. doi:10.1016/j.cell.2014.10.019

Schulz EG, Heard E. 2013. Role and control of X chromosome dosage in mammalian development. *Curr Opin Genet Dev* **23:** 109–115. doi:10.1016/j.gde.2013.01.008

Shankar SR, Bahirvani AG, Rao VK, Bharathy N, Ow JR, Taneja R. 2013. G9a, a multipotent regulator of gene expression. *Epigenetics* **8:** 16–22. doi:10.4161/epi.23331

Shibata S, Lee JT. 2004. Tsix transcription- versus RNA-based mechanisms in Xist repression and epigenetic choice. *Curr Biol* **14:** 1747–1754. doi:10.1016/j.cub.2004.09.053

Shinkai Y, Tachibana M. 2011. H3k9 methyltransferase G9a and the related molecule GLP. *Genes Dev* **25:** 781–788. doi:10.1101/gad.2027411

Silva J, Mak W, Zvetkova I, Appanah R, Nesterova TB, Webster Z, Peters AH, Jenuwein T, Otte AP, Brockdorff N. 2003. Establishment of histone h3 methylation on the inactive X chromosome requires transient recruitment of Eed-Enx1 polycomb group complexes. *Dev Cell* **4:** 481–495. doi:10.1016/S1534-5807(03)00068-6

Simon MD, Pinter SF, Fang R, Sarma K, Rutenberg-Schoenberg M, Bowman SK, Kesner BA, Maier VK, Kingston RE, Lee JT. 2013. High-resolution Xist binding maps reveal two-step spreading during X-chromosome inactivation. *Nature* **504:** 465–469. doi:10.1038/nature12719

Starmer J, Magnuson T. 2009. A new model for random X chromosome inactivation. *Development* **136:** 1–10. doi:10.1242/dev.025908

Stavropoulos N, Lu N, Lee JT. 2001. A functional role for Tsix transcription in blocking Xist RNA accumulation but not in X-chromosome choice. *Proc Natl Acad Sci* **98:** 10232–10237. doi:10.1073/pnas.171243598

Sunwoo H, Wu JY, Lee JT. 2015. The Xist RNA-PRC2 complex at 20-nm resolution reveals a low Xist stoichiometry and suggests a hit-and-run mechanism in mouse cells. *Proc Natl Acad Sci* **112:** E4216–E4225. doi:10.1073/pnas.1503690112

Sunwoo H, Colognori D, Froberg JE, Jeon Y, Lee JT. 2017. Repeat E anchors Xist RNA to the inactive X chromosomal compartment through CDKN1A-interacting protein (CIZ1). *Proc Natl Acad Sci* **114:** 10654–10659. doi:10.1073/pnas.1711206114

Tachibana M, Sugimoto K, Fukushima T, Shinkai Y. 2001. Set domain-containing protein, G9a, is a novel lysine-preferring mammalian histone methyltransferase with hyperactivity and specific selectivity to lysines 9 and 27 of histone H3. *J Biol Chem* **276:** 25309–25317. doi:10.1074/jbc.M101914200

Tachibana M, Sugimoto K, Nozaki M, Ueda J, Ohta T, Ohki M, Fukuda M, Takeda N, Niida H, Kato H, et al. 2002. G9a histone methyltransferase plays a dominant role in euchromatic histone H3 lysine 9 methylation and is essential for early embryogenesis. *Genes Dev* **16:** 1779–1791. doi:10.1101/gad.989402

Tachibana M, Ueda J, Fukuda M, Takeda N, Ohta T, Iwanari H, Sakihama T, Kodama T, Hamakubo T, Shinkai Y. 2005. Histone methyltransferases G9a and GLP form heteromeric complexes and are both crucial for methylation of euchromatin at H3-K9. *Genes Dev* **19:** 815–826. doi:10.1101/gad.1284005

Tachibana M, Matsumura Y, Fukuda M, Kimura H, Shinkai Y. 2008. G9a/GLP complexes independently mediate H3K9 and DNA methylation to silence transcription. *EMBO J* **27:** 2681–2690. doi:10.1038/emboj.2008.192

Trapnell C, Roberts A, Goff L, Pertea G, Kim D, Kelley DR, Pimentel H, Salzberg SL, Rinn JL, Pachter L. 2012. Differential gene and transcript expression analysis of RNA-seq experiments with TopHat and cufflinks. *Nat Protoc* **7:** 562–578. doi:10.1038/nprot.2012.016

Ule J, Jensen KB, Ruggiu M, Mele A, Ule A, Darnell RB. 2003. CLIP identifies Nova-regulated RNA networks in the brain. *Science* **302:** 1212–1215. doi:10.1126/science.1090095

Vedadi M, Barsyte-Lovejoy D, Liu F, Rival-Gervier S, Allali-Hassani A, Labrie V, Wigle TJ, Dimaggio PA, Wasney GA, Siarheyeva A, et al. 2011. A chemical probe selectively inhibits G9a and GLP methyltransferase activity in cells. *Nat Chem Biol* **7:** 566–574. doi:10.1038/nchembio.599

Velazquez Camacho O, Galan C, Swist-Rosowska K, Ching R, Gamalinda M, Karabiber F, De La Rosa-Velazquez I, Engist

B, Koschorz B, Shukeir N, et al. 2017. Major satellite repeat RNA stabilize heterochromatin retention of Suv39h enzymes by RNA-nucleosome association and RNA:DNA hybrid formation. *Elife* **6:** e25293. doi:10.7554/eLife.25293

Wang J, Mager J, Chen Y, Schneider E, Cross JC, Nagy A, Magnuson T. 2001. Imprinted X inactivation maintained by a mouse Polycomb group gene. *Nat Genet* **28:** 371–375. doi:10.1038/ng574

Wang CY, Jégu T, Chu HP, Oh HJ, Lee JT. 2018. SMCHD1 merges chromosome compartments and assists formation of superstructures on the inactive X. *Cell* **174:** 406–421.e25. doi:10.1016/j.cell.2018.05.007

Wutz A. 2011. Gene silencing in X-chromosome inactivation: advances in understanding facultative heterochromatin formation. *Nat Rev Genet* **12:** 542–553. doi:10.1038/nrg3035

Yokochi T, Poduch K, Ryba T, Lu J, Hiratani I, Tachibana M, Shinkai Y, Gilbert DM. 2009. G9a selectively represses a class of late-replicating genes at the nuclear periphery. *Proc Natl Acad Sci* **106:** 19363–19368. doi:10.1073/pnas.0906142106

Zhang LF, Huynh KD, Lee JT. 2007. Perinucleolar targeting of the inactive X during S phase: evidence for a role in the maintenance of silencing. *Cell* **129:** 693–706. doi:10.1016/j.cell.2007.03.036

Zhang Y, Liu T, Meyer CA, Eeckhoute J, Johnson DS, Bernstein BE, Nussbaum C, Myers RM, Brown M, Li W, et al. 2008. Model-based analysis of ChIP-seq (MACS). *Genome Biol* **9:** R137. doi:10.1186/gb-2008-9-9-r137

Zhao J, Sun BK, Erwin JA, Song JJ, Lee JT. 2008. Polycomb proteins targeted by a short repeat RNA to the mouse X chromosome. *Science* **322:** 750–756. doi:10.1126/science.1163045